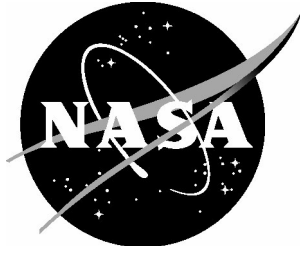NASA/TM–20240000025

Direct Numerical Simulation of Smooth-Body Flow Separation Around a Ramp

Ali Uzun
Analytical Mechanics Associates, Hampton, Virginia

Mujeeb R. Malik
Langley Research Center, Hampton, Virginia

January 2024

NASA STI Program Report Series

Since its founding, NASA has been dedicated to the advancement of aeronautics and space science. The NASA scientific and technical information (STI) program plays a key part in helping NASA maintain this important role.

The NASA STI program operates under the auspices of the Agency Chief Information Officer. It collects, organizes, provides for archiving, and disseminates NASA's STI. The NASA STI program provides access to the NTRS Registered and its public interface, the NASA Technical Reports Server, thus providing one of the largest collections of aeronautical and space science STI in the world. Results are published in both non-NASA channels and by NASA in the NASA STI Report Series, which includes the following report types:

- TECHNICAL PUBLICATION. Reports of completed research or a major significant phase of research that present the results of NASA Programs and include extensive data or theoretical analysis. Includes compilations of significant scientific and technical data and information deemed to be of continuing reference value. NASA counterpart of peer-reviewed formal professional papers but has less stringent limitations on manuscript length and extent of graphic presentations.

- TECHNICAL MEMORANDUM. Scientific and technical findings that are preliminary or of specialized interest, e.g., quick release reports, working papers, and bibliographies that contain minimal annotation. Does not contain extensive analysis.

- CONTRACTOR REPORT. Scientific and technical findings by NASA-sponsored contractors and grantees.

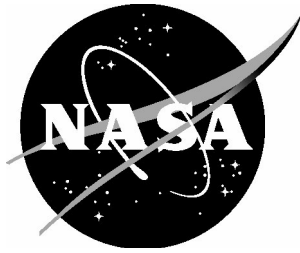- CONFERENCE PUBLICATION. Collected papers from scientific and technical conferences, symposia, seminars, or other meetings sponsored or co-sponsored by NASA.

- SPECIAL PUBLICATION. Scientific, technical, or historical information from NASA programs, projects, and missions, often concerned with subjects having substantial public interest.

- TECHNICAL TRANSLATION. English-language translations of foreign scientific and technical material pertinent to NASA's mission.

Specialized services also include organizing and publishing research results, distributing specialized research announcements and feeds, providing information desk and personal search support, and enabling data exchange services.

For more information about the NASA STI program, see the following:

- Access the NASA STI program home page at http://www.sti.nasa.gov

- Help desk contact information:

https://www.sti.nasa.gov/sti-contact-form/
and select the "General" help request type.

Direct Numerical Simulation of Smooth-Body Flow Separation Around a Ramp

Ali Uzun
Analytical Mechanics Associates, Hampton, Virginia

Mujeeb R. Malik
Langley Research Center, Hampton, Virginia

January 2024

Direct Numerical Simulation of Smooth-Body Flow Separation Around a Ramp

Ali Uzun

Analytical Mechanics Associates, Hampton, Virginia 23666

Mujeeb R. Malik

NASA Langley Research Center, Hampton, Virginia 23681

Abstract

Spanwise-periodic computation of a turbulent flow past a two-dimensional smooth ramp geometry is performed in the form of a direct numerical simulation. The Reynolds number based on the ramp height is about $147,000$. A straight section that precedes the smooth ramp allows the incoming turbulent boundary layer to grow under a weak favorable pressure gradient. The boundary layer introduced at the domain inlet has a momentum-thickness based Reynolds number of 2000. The turbulent boundary layer nearing the ramp first interacts with a relatively stronger favorable pressure gradient, followed by a strong adverse pressure gradient. Consequently, the boundary layer experiences a modest acceleration before decelerating and separating. Analysis of the data over this region hints at the formation of an internal layer beneath the accelerated boundary layer. The analysis also reveals that this internal layer forms the origin of the free shear layer that emerges in the deceleration region and separates. The streamwise extent of the separated region is comparable to the ramp length, while the viscous layer thickness near reattachment is about the same as the ramp height; hence, the boundary layer undergoing separation and subsequent reattachment in the present configuration experiences its thickness being amplified by about tenfold. The reattached flow continues to develop further under a diminishing pressure gradient in the recovery region in a similar fashion to a zero pressure gradient turbulent boundary layer.

Nomenclature

C	=	logarithmic layer intercept constant
C_f	=	time- and spanwise-averaged skin-friction coefficient
C_p	=	mean surface pressure coefficient
h	=	ramp height
H	=	boundary-layer shape factor
L	=	ramp length
n	=	wall-normal distance
p	=	pressure
Re_L	=	Reynolds number based on L, $\rho_r U_r L / \mu_r$
u	=	streamwise velocity component in the local orthogonal coordinate system
u_τ	=	wall friction velocity
U	=	mean streamwise velocity component in the local orthogonal coordinate system
v	=	wall-normal velocity component in the local orthogonal coordinate system
v_i	=	velocity component in the Cartesian coordinate system, where $i = 1, 2, 3$
w	=	spanwise velocity component
x	=	axial direction

y	=	vertical direction
z	=	spanwise direction
α_f	=	filtering parameter
δ	=	boundary-layer thickness
δ^*	=	displacement thickness
Δn	=	grid spacing along the local wall-normal direction
Δs	=	grid spacing along the local streamwise direction
Δz	=	spanwise grid spacing; separation distance in two-point correlations
κ	=	von Kármán constant
μ	=	molecular viscosity
ν	=	kinematic viscosity, μ/ρ
ρ	=	fluid density
τ	=	viscous shear stress
θ	=	momentum thickness
$\langle\ \rangle$	=	temporal and spanwise averaging operator

Subscripts

e	=	boundary-layer edge value
r	=	reference value
w	=	value on wall
θ	=	momentum-thickness based value

Superscripts

$\prime$	=	perturbation from mean value
$+$	=	value in wall units

1 Introduction

Successful cost-effective prediction of practical high Reynolds number turbulent flows that encounter a strong pressure gradient, surface curvature effects, and subsequently undergo separation remains a pacing item in turbulence research. While wall-modeled large-eddy simulation (WMLES) techniques appear to have emerged as the most appropriate choice for this challenging task, several unresolved issues related to this particular type of simulation methodology persist and require further investigation. Some of these issues include: a) determination of the optimal exchange location between the wall model employed in the near-wall layer, and the outer region where traditional LES is applied; b) dynamic variation of the exchange location in response to the changes in outer region flow conditions; c) better understanding of the interplay between the LES subgrid-scale (SGS) model and the wall model; d) determination of the required outer region grid resolution to provide a reasonably accurate input to the wall model, which would depend on the specifics of the numerical discretization scheme as well as the SGS model employed. Hence, the best practices needed for routine applications of WMLES to practical problems still remain to be established.

To further evaluate the use of WMLES in flows involving separation, the AIAA LES Discussion Group devised a canonical problem that investigates the smooth-body flow separation around a two-dimensional ramp geometry under assumed spanwise-periodicity conditions. The problem involves the separation of an incoming turbulent boundary layer after it experiences the adverse pressure gradient generated by the ramp profile, as depicted in Figure 1. The present canonical problem can be considered as one of the simplest configurations that generates complex enough physics involving smooth-body flow separation, and hence poses a reasonable challenge for turbulence-modeling efforts. The relatively simple geometry also makes the problem tractable by many different flow solvers. It should be noted that this particular setup is a simplification of the experimental configuration of Simmons et al. [1], who investigated the three-

dimensional flow separation around an identical ramp profile. The experimental flow included the additional complications introduced by the finite model span and the presence of tunnel side walls. It was found that although the flow separation was highly three-dimensional, the reattachment was spanwise uniform. The surface flow topology observed in that experiment was characterized by an "owl-face pattern of the fourth kind" [1], similarly observed in separated flows around inclined bodies of revolution. Although the simpler canonical setup does not replicate all features of the rather complex experimental flow, it can be considered as a useful stepping-stone case in which WMLES approaches can be evaluated and properly validated, before they are applied to more complicated flows with confidence.

The 2022 High Fidelity CFD Verification Workshop had 11 participant teams who submitted WMLES results for the smooth ramp flow [2]. As the workshop did not have any truth data for comparison, the WMLES studies had to be performed in an essentially blind manner without being able to fine tune the turbulence model parameters and the grid details in order to best match any available validation data. The comparison of the WMLES results against one another showed a large spread among the results, and raised valid concerns about the maturity level of WMLES. Given these observations, it seems hard to have full confidence in the true predictive capability of WMLES where it matters, i.e., in situations where results are needed with a relatively quick turnaround for a problem for which no other simulation or experimental data exist.
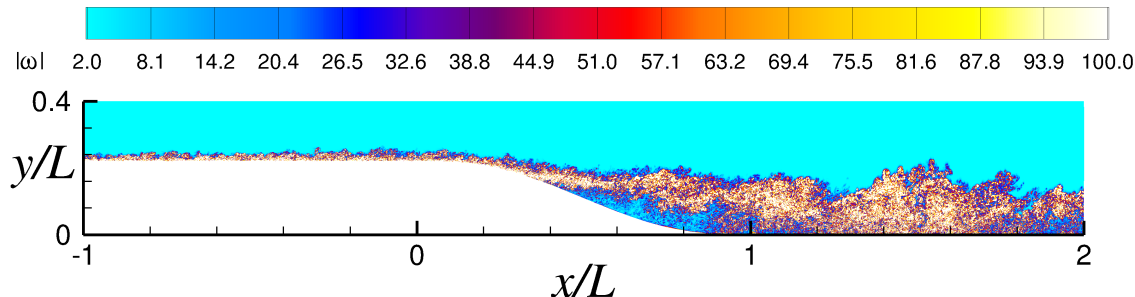

Figure 1. Flow separation induced by adverse pressure gradient around the smooth ramp geometry. Contours denote the instantaneous normalized total vorticity magnitude on an $x - y$ plane.

To support the planned work on further investigations of WMLES in the smooth ramp flow, and in consultation with the 2022 High Fidelity CFD Verification Workshop organizers, we have performed a direct numerical simulation (DNS) of the problem under assumed spanwise-periodicity conditions. The primary goal of this DNS is to generate a dataset that can serve as the truth data for the related WMLES studies. We anticipate that this dataset will provide guidance toward resolving some of the pending issues in WMLES. This document provides the computational setup and other details of the DNS, and an analysis of the results along with the key findings. The data from the DNS, along with this paper, are being made available to the community after the completion of the follow-up blind test challenge study in January 2024.

We should note that the community has also been engaged in a similar problem known as the "speed-bump flow," which involves the interaction of an incoming turbulent boundary layer with the strong favorable and adverse pressure gradients generated by a Gaussian bump [3]. Experimental measurements [4, 5, 6, 7] as well as high-fidelity simulation results [8, 9, 10] of that case are readily available for the validation of lower-fidelity simulation tools. The strong favorable pressure gradient over the windward side of the speed bump leads to strong flow acceleration and generation of an internal layer beneath the strongly accelerated boundary layer. The thickness of this internal layer falls within the typical wall-modeled portion of a boundary layer in a WMLES [10]. Furthermore, this internal layer evolves into the detached shear layer that emerges over the leeward side of the bump due to the strong adverse pressure gradient. Hence, the presence of an internal layer in the speed-bump flow presents additional challenges for wall-modeling.

For the ramp flow, it was originally envisaged that the straight development section used upstream of the ramp would eliminate the generation of an internal layer. However, the findings from our analysis hint at the formation of an internal layer beneath the boundary layer during the brief acceleration period over the early ramp section, due to the presence of a relatively strong favorable pressure gradient in that region. The analysis also suggests that the internal layer generated over the brief acceleration region forms the origin of the free shear layer that emerges in the deceleration region and separates. Whether this particular feature of the ramp flow will create any challenges for WMLES remains to be seen. This document is organized as follows. Section 2 gives the details of the computational methodology used in the DNS. Simulation details and the analysis of the simulation results are provided in section 3. Section 4 summarizes the findings and provides the concluding remarks.

2 Computational methodology

The code used for the simulation solves the unsteady three-dimensional compressible Navier-Stokes equations discretized on multiblock structured and overset grids. For the present simulation, a single-block grid is used because of the simple geometry. The code employs an optimized prefactored fourth-order accurate compact finite-difference scheme [11] to compute all spatial derivatives in the governing equations. This optimized scheme offers improved dispersion characteristics compared to the standard sixth- and eighth-order compact schemes [12]. It is derived from the standard eighth-order compact scheme that has been shown to possess "spectral-like" resolution [12]. Third-order one-sided and biased schemes, respectively, are used on a boundary point and on the point next to the boundary. To eliminate the spurious high-frequency numerical oscillations that may arise from several sources and to ensure numerical stability, we also employ high-order (up to tenth-order) compact filtering schemes [13, 14]. The present simulation uses the tenth-order filtering scheme, with matching one-sided biased formulations near the physical boundaries [13]. A Beam-Warming type approximately factorized implicit scheme with subiterations is used for the time advancement [15]. The block tridiagonal systems that arise from the application of the time discretization scheme are solved directly along each spatial direction successively. Three subiterations per time step are applied to drop the residuals by two orders of magnitude, which is sufficient to maintain the time accuracy, based on our experience. More details of the simulation methodology can be found in the earlier publications by Uzun and coworkers [16, 17, 18, 19].

3 Spanwise-periodic flow simulation over the smooth ramp geometry at $Re_L = 0.667$ million

The smooth ramp profile is described by

$$\frac{y}{L} = \frac{h}{L}\left[1 - 10\left(\frac{x}{L}\right)^3 + 15\left(\frac{x}{L}\right)^4 - 6\left(\frac{x}{L}\right)^5\right] \qquad (1)$$

where x, y, z, respectively, denote the axial, vertical and spanwise directions, L is the ramp length that is taken as the reference length scale, and $h = 0.22L$ is the ramp height. The ramp profile begins at $(x, y) = (0, h)$ and ends at $(x, y) = (L, 0)$. The sections upstream and downstream of the ramp are straight segments, as depicted in Figure 1.

To avoid confusion in the upcoming discussion, we should clarify the distinction between the axial and streamwise directions. The streamwise direction is defined in the local orthogonal coordinate system relative to the ramp surface, and represents the direction perpendicular to the local surface normal (or the direction parallel to the local surface tangent), while the axial direction is the same as the x direction of the Cartesian coordinate system. In the straight sections upstream and downstream of the ramp, the two directions are obviously identical.

4

3.1 Simulation details

The Reynolds number based on the inlet reference velocity, U_r, and L is $Re_L = 0.667$ million, while the inlet Mach number is set to 0.2. The corresponding Reynolds number based on h is about $147,000$. The incoming boundary-layer thickness is $\delta_{in} = 0.024L$, giving a ratio between the inlet boundary-layer thickness and the ramp height of $\delta_{in}/h \approx 0.11$. The periodic domain span is set to $12\delta_{in} = 0.288L$. The Reynolds numbers based on the inlet boundary-layer thickness and the corresponding momentum thickness are $Re_\delta = 16,000$ and $Re_\theta = 2000$, respectively. A schematic of the computational domain is provided in Figure 2. The inflow boundary is at $x/L = -1$ while the outflow boundary is at $x/L = 7$. The physical domain ends at $x/L = 4$. The region from $x/L = 4$ to 7 is the sponge zone, where the grid is highly stretched in the axial direction. This region therefore contains only a few hundred points in the axial direction. The sponge zone damps out the turbulence before it reaches the outflow boundary, where standard characteristic outflow boundary conditions are applied with a specified back pressure. Viscous adiabatic boundary conditions are imposed on the lower wall that contains the ramp profile. The top boundary is a straight segment placed at $y/L = 0.74$, on which an inviscid wall condition is applied. Since this is an internal flow problem, the back pressure on the outflow boundary has to be set to 1.013 times the inlet pressure in order to obtain a Mach number of 0.2 at the inlet. This value was determined via precursor wall-resolved large-eddy simulations (WRLES) performed on a coarsened grid.
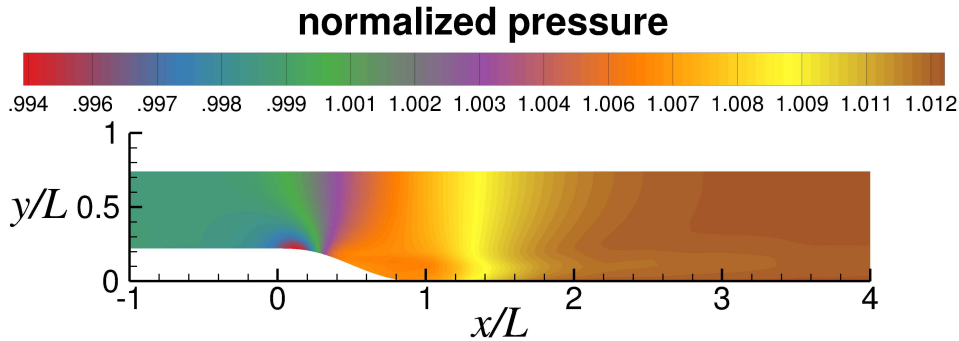

Figure 2. Computational domain schematic. Contours denote the mean pressure normalized by the reference value. Note that the sponge zone downstream of the physical domain is omitted here.

The domain is discretized using a single block grid comprised of $12,544$ points along the streamwise direction and 1600 uniform points along the spanwise direction. The number of points along the grid lines running between the lower and upper walls is 512. Figure 3 plots the variation of streamwise, wall-normal and spanwise grid resolutions in terms of wall units, respectively, denoted as Δs^+, Δn^+ and Δz^+, along the lower wall. These are determined using the local wall friction velocity. Upstream of the ramp, $\Delta s^+ < 10$ generally, while Δz^+ maintains a value of about 5. Once the flow starts interacting with the relatively strong favorable pressure gradient over the initial ramp section, Δs^+ and Δz^+ increase toward 10.5 and 5.4, respectively, because of the increasing skin friction in that region. These spacings quickly decrease as the flow decelerates toward separation. The largest values of Δs^+ and Δz^+ within the separated region are about 3.8 and 1.8, respectively. The separated flow region, which is about $1.07L$ in length, is covered by about 3000 points along the streamwise direction. The average thickness of the viscous layer between the separation and reattachment points is $\delta_{avg} \approx 0.17L$, which is based on the integrated value of δ between the separation and reattachment locations. The average streamwise spacing in the separated region therefore corresponds to about $\delta_{avg}/477$, which represents a relatively fine resolution. The spanwise spacing within the separated region is about half of the streamwise spacing. Once the flow recovers from the separation, Δs^+ and Δz^+ start to increase in tandem with the rising skin friction. Toward the end of the physical domain, the largest Δs^+ and Δz^+ become about 8.8 and 3.2, respectively.

5

The wall-normal grid spacing, Δn^+, on the wall is generally smaller than 1 in the attached region and decreases in the separated region. Δn^+ increases with distance from the wall via a mild grid stretching factor. In the attached region prior to separation, the largest Δn^+ in the vicinity of the boundary-layer edge is around 10–12 units. Once the flow decelerates toward separation, the corresponding boundary-layer edge values decrease toward 1–2 at the separation point. In the downstream recovery region, the largest Δn^+ values around the boundary-layer edge are found near the end of the physical domain, and have a value of about 40. These outer region spacings get relatively larger in the recovery region because the reattached boundary layer is considerably thicker than that prior to separation. Also, as will be seen, the outer part of the recovery region flow contains the remnants of the large-scale structures generated in the separated region; hence, such wall-normal spacings in that part of the recovery flow are not of particular concern. There are about 300 points from the wall to the outer edge of the free shear layer at the beginning of flow separation. The thickest section of the separated flow region contains around 400 out of the total 512 points in the vertical direction.
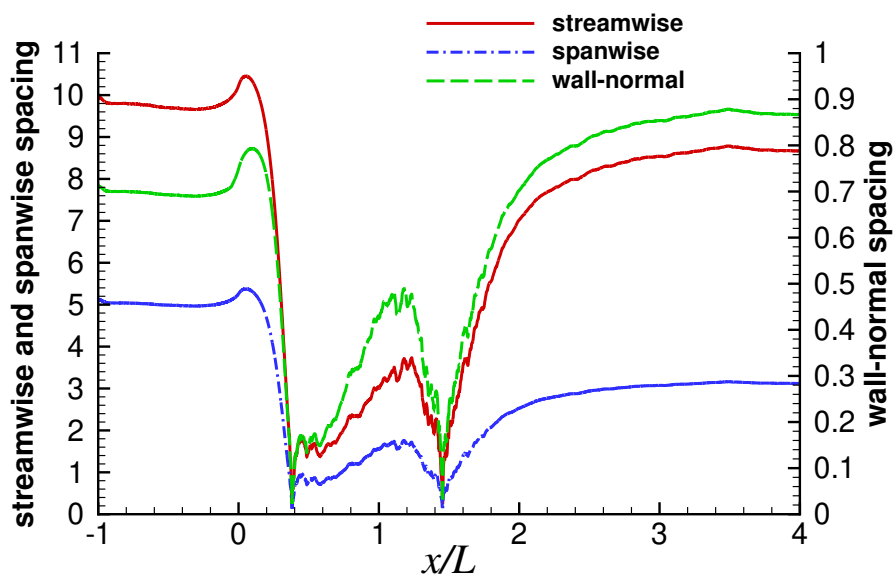

Figure 3. Near-wall grid spacings in inner units along the lower wall.

The second-order accurate implicit Beam-Warming scheme [15] is used for the time integration. The time step taken in the simulation corresponds to a maximum CFL number of about 5. This value is based on the sum of the acoustic speed and the local flow velocity. It takes $50,000$ time steps to compute a time interval of L/U_r. To maintain numerical stability, the solution is filtered at every time step using the tenth-order compact filter with a filtering parameter of $\alpha_f = 0.49$ [13, 14], which is known to provide a minimal amount of numerical dissipation from an earlier study [20]. To minimize the duration of the initial transient period, the simulation is started from the solution available from a precursor WRLES performed on a coarser grid. The initial conditions of the WRLES, on the other hand, are generated by adding randomized disturbances onto the mean flowfield solution obtained from a RANS calculation. The initial numerical transients of the DNS are driven out of the computational domain during the first $12L/U_r$. Statistical data are gathered over the next $10.2L/U_r$, which covers 2.04 physical domain flow-through times.

For the turbulent inflow generation, we employ the rescaling-recycling technique described in Uzun and Malik [21, 8, 10]. Our method only recycles the velocity fluctuations while keeping the mean inflow profile fixed. The fluctuations are generated using the recycling/rescaling with dynamic reflection (RR+DR) technique introduced by Morgan et al. [22]. In this procedure, a reflection about a randomly chosen spanwise plane is applied to the scaled fluctuations extracted from the recycle plane before introducing them at the

inflow plane. The spanwise reflection plane is updated at certain randomized intervals using the same procedure as described by Morgan et al. [22]. The mean flow imposed at the inflow boundary is taken from the DNS of Schlatter and Örlü [23] at $Re_\theta = 2000$ for a zero pressure gradient turbulent boundary layer. The mean inflow boundary-layer thickness at $x/L = -1$ is $\delta_{in} = 0.024L$. Since turbulence intensity profiles are also available from the same DNS [23], those profiles are used in the rescaling of the velocity fluctuations extracted from the recycle plane. In this way, the time and spanwise averages of the rescaled fluctuations introduced at the inlet match the imposed turbulence intensity profiles. The distance between the inflow and recycle planes is $10\delta_{in}$. To verify that the method generates realistic boundary-layer development, Figure 4 shows the comparison of the mean streamwise velocity and turbulence intensity profiles in wall units at $x/L = -0.3$, where $Re_\theta = 2485$, with the flat plate boundary-layer DNS of Schlatter and Örlü [23] at a similar value of $Re_\theta = 2540$. We note that $Re_\theta = 2485$ is the highest value reached upstream of the ramp. We find reasonable overall agreement for all profiles. The skin-friction coefficient of our profile is about 4% higher. The differences in the mean velocity and turbulence intensity profiles are believed to mainly arise from the favorable pressure gradient effect near the ramp, and from the different numerics between the two simulations to a certain extent. Our profile's relatively higher skin-friction coefficient is also consistent with the favorable pressure gradient effect near the ramp, and the slightly lower Re_θ of the present case.
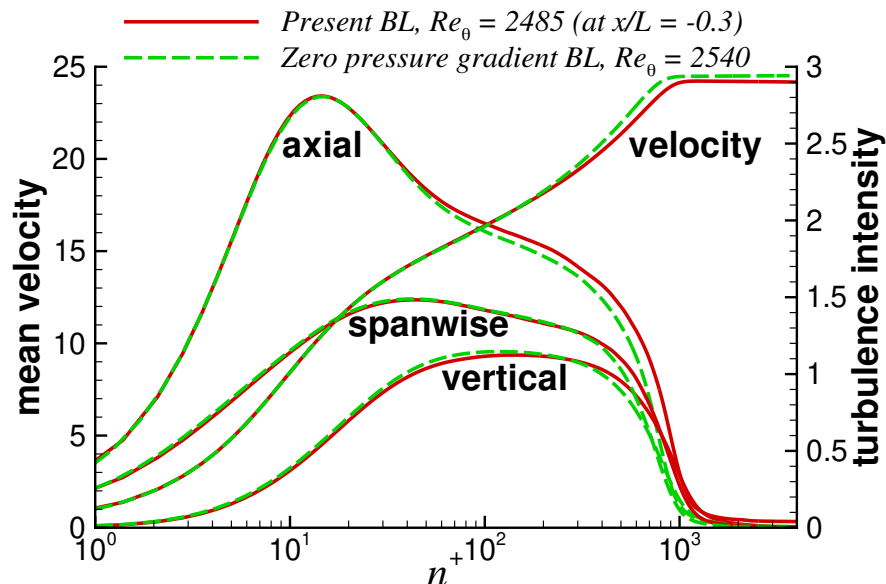

Figure 4. Mean velocity and turbulence intensity comparisons with the data from Ref. [23].

3.2 Simulation results

We now discuss the main findings. As depicted earlier in Figure 1, the flow separation due to the adverse pressure gradient generated by the ramp profile is illustrated by the free shear layer represented by high levels of vorticity, and the reversed flow region beneath this shear layer, which contains relatively lower vorticity levels. The subsequent reattachment of the separated flow generates a much thicker boundary layer compared to that prior to separation. Figure 5 shows the separated region in terms of the mean flow stream-lines superimposed on the normalized mean axial velocity contours. The streamwise extent of the separated region almost equals the ramp length, while the boundary-layer thickness near reattachment is comparable to the ramp height. Hence, the boundary layer undergoing separation and subsequent reattachment in the present configuration experiences its thickness being amplified by about tenfold.

3.2.1 Main flowfield features

The variation of several quantities that are representative of the main flowfield features is examined first. The quantities of interest are the mean boundary-layer thickness, δ, its corresponding displacement and momentum thicknesses, denoted as δ^* and θ, respectively, the shape factor $H = \delta^*/\theta$, and the boundary-layer edge velocity, U_e, which is normalized by the inlet reference velocity, U_r. All boundary-layer thicknesses are scaled by L. Surface pressure and skin-friction coefficients on the lower wall are the other quantities of interest. These coefficients are given by

$$C_p = \frac{p - p_r}{\frac{1}{2}\rho_r U_r^2} \quad \text{and} \quad C_f = \frac{\tau_w}{\frac{1}{2}\rho_r U_r^2} \tag{2}$$

where ρ_r, p_r, U_r, respectively, are the inlet density, pressure and velocity, which are taken as the reference values, p is the mean surface pressure and τ_w is the mean wall shear stress.
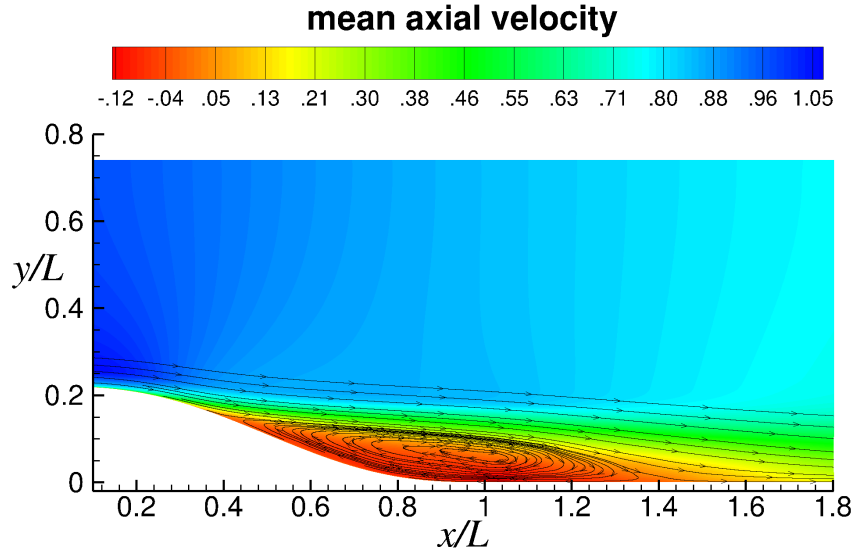
Figure 5. Mean flow streamlines depicting the separated flow region.

To determine δ, we use the method proposed by Griffin et al. [24], which is based on the local reconstruction of an inviscid velocity profile along the wall-normal direction using the Bernoulli equation. In this method, the boundary-layer thickness is defined as the location at which $U/U_I = m/100$, where U is the actual local streamwise velocity at a given wall-normal distance, U_I is the inviscid velocity reconstructed using the proposed procedure, and m is the percentage value that determines the edge of the boundary layer. It is chosen as 99.5 here. To compute δ^* and θ, we use the classical definitions of displacement and momentum thicknesses based on the integrals of streamwise velocity. The integrals are truncated at the wall-normal distance corresponding to the edge of the local boundary layer. The methods used here to determine the boundary-layer thickness and related quantities do not distinguish between attached and separated flows. Although the concept of a boundary-layer thickness in the separated region is rather vague, we consider the boundary-layer structure in that region to be comprised of the free shear layer and the reversed flow region beneath it. The boundary-layer edge in the separated region represents the outer edge of the shear layer.

Figure 6 plots the variation of δ/L, δ^*/L, θ/L, shape factor, $H = \delta^*/\theta$, U_e, C_p and C_f. All quantities experience significant changes as the flow travels from the domain inlet to the end of the physical domain. The incoming boundary layer encounters an initially mild favorable pressure gradient far upstream of the ramp, as indicated by the C_p variation there, and the corresponding gradual increase in U_e. Over the same region, the boundary layer also experiences a linear growth in δ, δ^* and θ, accompanied by the related gradual

8

drop in C_f. Note that the C_f variation depicts a brief transient behavior near the inlet over a few incoming boundary-layer thicknesses due to transients associated with the turbulent inflow generation method. The boundary-layer shape factor, H, over the upstream region is about 1.4, and compares favorably with the typical values of 1.3–1.4 expected for a zero pressure gradient fully developed turbulent boundary layer. The upstream favorable pressure gradient becomes relatively stronger in the vicinity of $x/L = -0.2$ and persists over the early ramp section. This causes the increases in U_e and C_f over that segment. The accelerated flow sees a modest increase in U_e, which takes a maximum value of about $1.055U_r$ at $x/L \approx 0.105$. The flow acceleration increases the C_f because of the steepening near-wall velocity gradient. We find that the C_f peak is at $x/L \approx 0.055$, while that of C_p is at $x/L \approx 0.12$. Although the flow acceleration caused by the favorable pressure gradient over the early ramp section is not strong enough to have a noticeable thinning effect on δ, it causes a reduction in δ^* and θ, because of the changes occurring in the mean boundary-layer profile shape. We also observe that the reductions in δ^* and θ take place at different rates, and θ decreases at a faster rate than that of δ^*. This creates a local maximum value of $H = 2.7$ at $x/L \approx 0.156$.
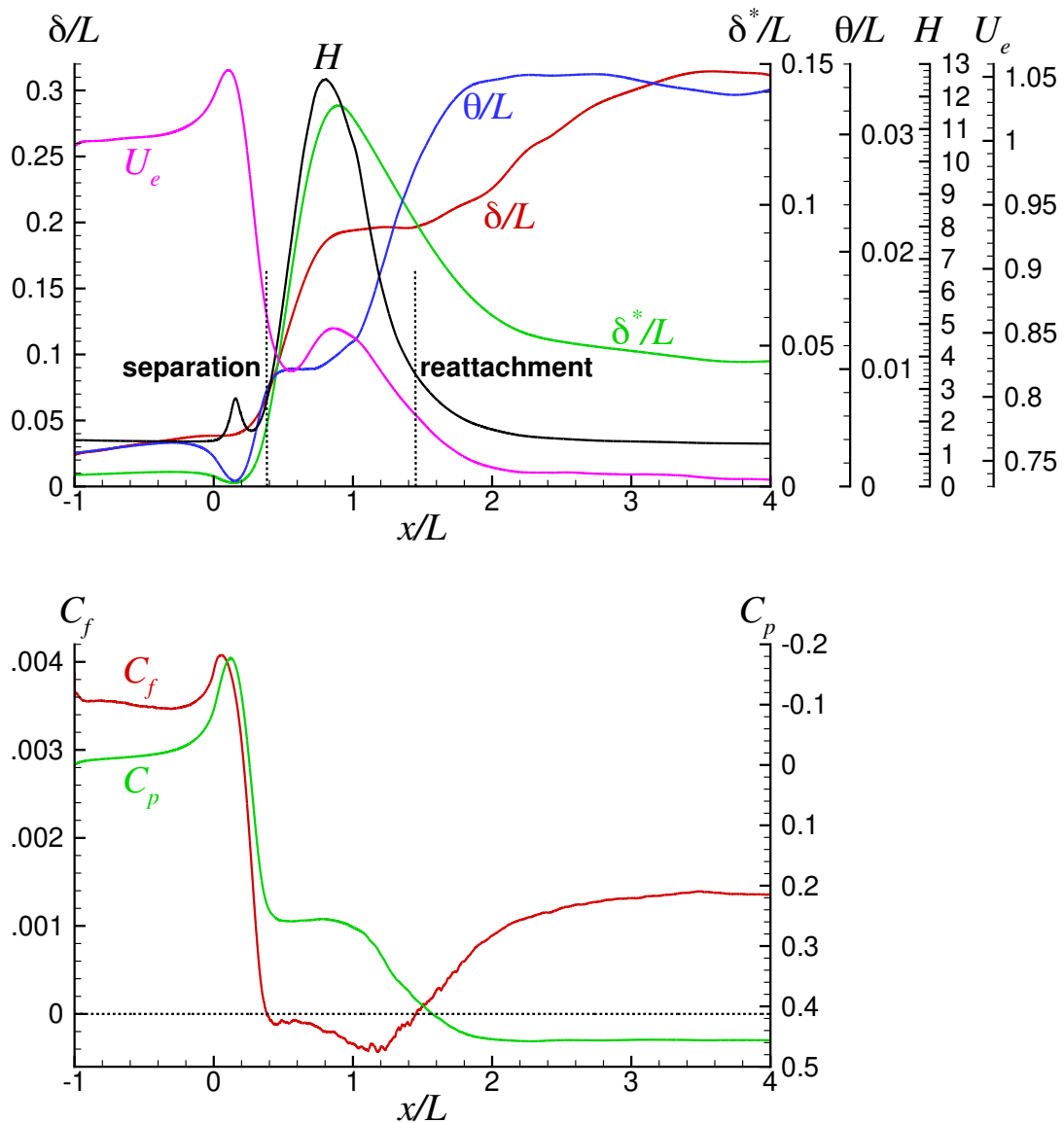

Figure 6. Streamwise variation of δ/L, δ^*/L, θ/L, H, U_e, C_p and C_f.

9

After passing through the favorable pressure gradient region over the early ramp section, the flow encounters the adverse pressure gradient and begins to slow down. This deceleration leads to the onset of separation at about $x/L = 0.38$. The deceleration lowers U_e considerably from its peak value that was generated in the upstream acceleration region. The flow separation is indicated by the negative C_f distribution, which depicts a fairly broad reversed flow region, and the associated plateau in the C_p distribution within that region. The horizontal extent of the separated region is comparable to the ramp length. We also see that U_e attains a secondary peak that is roughly in the middle of the separated region. U_e starts to decrease once more as the separated shear layer passes over the recirculating region and moves toward reattachment, which is at $x/L = 1.45$, and the wall pressure starts to rise downstream of the plateau seen in the C_p distribution at the same time. The pressure gradient remains negligible as the recovery flow evolves further downstream, while U_e initially stays constant and then starts to gradually decrease further downstream.

The boundary-layer thickness increases in the deceleration region and continues to do so after the flow separates. To reiterate, the separation occurs at $x/L = 0.38$. We see that δ continues to grow until $x/L \approx 0.9$ and then remains fairly steady until the reattachment at $x/L = 1.45$. δ within the plateau region is about 0.19–$0.2L$, which is comparable to the ramp height of $0.22L$. The separated flow generates large structures, whose reattachment leads to the further growth of a thick boundary layer in the recovery zone, as depicted in Figure 1. The associated growths in δ^* and θ, as the flow decelerates and separates, generate a peak value of $H = 12.5$ at $x/L \approx 0.8$, which is just before the start of the plateau in δ. The change in the mean velocity profile shape induced by the adverse pressure gradient causes a faster rate of increase in δ^* compared to that of θ, and this creates the large peak value of H. It is also interesting to note that θ plateaus from shortly after separation until $x/L \approx 0.75$, before resuming its growth, while δ^* monotonically increases to just after the global peak location in H. Shortly after the global H peak, δ^* begins to decrease while θ continues to increase, and both quantities start to stabilize once the flow reattaches and the recovery begins. Once again, these differences in the behavior between δ^* and θ as the flow undergoes separation and reattachment arise from the significant changes happening to the mean velocity profile shapes. Those mean velocity profiles will be examined in the later analysis. We see that H decreases substantially from its peak value as the separated flow reattaches. As the recovery flow evolves, H drops toward 1.3, which agrees well with the typical values of 1.3–1.4 expected for a zero pressure gradient turbulent boundary layer.

3.2.2 Examination of the region upstream of separation

We now examine the region upstream of separation. In this region, the incoming boundary layer first interacts with the weak favorable pressure gradient upstream of the ramp. The boundary layer then encounters a relatively stronger favorable pressure gradient over the early ramp section, which accelerates the flow prior to its entrance into the adverse pressure gradient region. The adverse pressure gradient decelerates the boundary layer and causes it to detach from the wall.

Figure 7 depicts the mean streamwise velocity profiles in wall units at several stations upstream of the ramp, where $-0.9 \leq x/L \leq -0.2$. Here, $n^+ = n u_\tau / \nu_w$ and $U^+ = U/u_\tau$, where n is the wall-normal distance, U is the mean streamwise velocity, $u_\tau = \sqrt{\tau_w/\rho_w}$ is the wall friction velocity, τ_w is the wall shear stress, and ρ_w and ν_w, respectively, are the density and kinematic viscosity on the wall. Over this region, the incoming turbulent boundary layer grows under a weak favorable pressure gradient, as indicated by the C_p distribution shown in Figure 6. We see that these mean velocity profiles in wall units show a good collapse in the inner region of the boundary layer, which is comprised of the viscous sublayer (i.e., $U^+ = n^+$ valid until $n^+ \approx 5$), the buffer zone (region from $5 \lesssim n^+ \lesssim 30$) and the logarithmic layer defined as $U^+ = \kappa^{-1} \ln(n^+) + C$. A von Kármán constant of $\kappa = 0.41$ together with an intercept constant of $C = 5.2$ is shown to be a good fit to the logarithmic layer of these profiles. The present κ and C values agree well with the typical values expected for zero pressure gradient turbulent boundary layers. The range of the logarithmic region gradually increases as the boundary layer grows in the upstream development region under the weak favorable pressure gradient.

We find that the weak favorable pressure gradient upstream of the ramp does not have much of an effect on the law-of-the-wall region or the logarithmic-layer properties. The wake region of the profiles respond to the boundary-layer growth and the increasing favorable pressure gradient effect (due to presence of ramp and top wall) as the flow approaches the ramp. Recall that the earlier comparison between our profile at $x/L = -0.3$, corresponding to $Re_\theta \approx 2500$, with a zero pressure gradient turbulent boundary layer at similar Re_θ, presented in Figure 4, shows some differences in the outer part of the boundary layer. Those differences are believed to be primarily due to the favorable pressure gradient effect near the ramp. As noted earlier, the C_f distribution exhibits a short transient section near the inlet boundary because of the transients associated with the turbulent inflow generation method. We see that the profile shown at $x/L = -0.9$ in Figure 7, which is located about 4 inlet boundary-layer thicknesses from the inlet, has a good collapse of its law-of-the-wall region onto the other stations taken further downstream. This observation suggests that the transient effects near the inlet boundary are confined to a relatively short section.
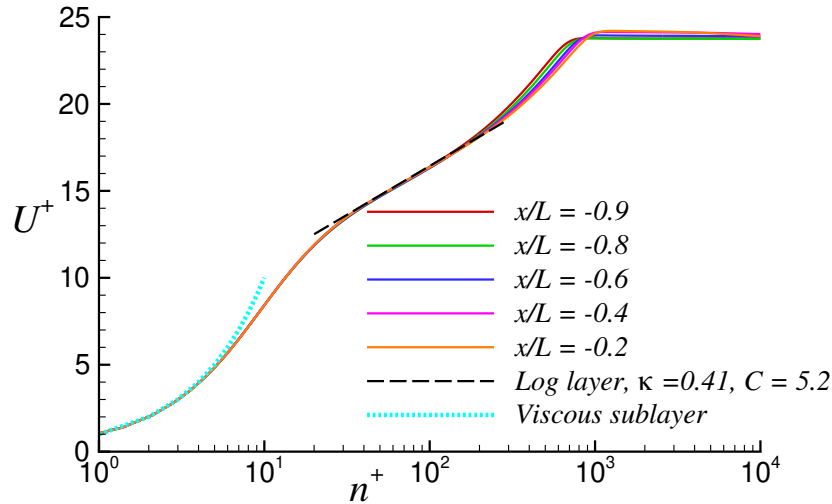
Figure 7. Mean streamwise velocity profiles in wall units in the region where $-0.9 \leq x/L \leq -0.2$.

The favorable pressure gradient gets stronger in the vicinity of $x/L = -0.2$, and persists over the early ramp section; this causes the boundary layer to accelerate in response. Figure 8 shows the mean velocity profiles in inner and outer units from the start of the strong favorable pressure gradient at $x/L = -0.2$ to $x/L = 0.12$, where the C_p peak is located. The acceleration due to the favorable pressure gradient increases the velocity magnitudes within the boundary layer and the edge velocity, as depicted in Figure 8(a). Because of the presence of a top wall and mass conservation, the outermost region of the profiles (beyond about 3δ) show a decrease in the velocity magnitude with increasing wall distance. The same mean velocity profiles plotted in inner units, on the other hand, show a good collapse of the law-of-the-wall region and the logarithmic layer over the range where $-0.2 \leq x/L \leq 0$, as seen in Figure 8(b). The logarithmic layer then shows a small upward shift as the flow reaches the C_f peak station at $x/L = 0.055$, continues to shift further as the C_p peak is reached at $x/L = 0.12$. Similar upward shifts of the logarithmic layer in strongly-accelerated nonrelaminarizing flows have been observed in experimental studies [25], as well as in our prior studies of the speed-bump flow [10], which features a rather strong favorable pressure gradient region over an extended region. In such accelerated boundary layers, the extent of the logarithmic layer shift and how soon it begins depend on the strength of the favorable pressure gradient, and its streamwise extent.

Figure 9 plots the power spectral density (PSD) of the axial velocity fluctuations versus the Strouhal frequency, $Sr = fL/U_r$ (where f is the frequency), within the turbulent boundary layer at $x/L = -0.62, -0.25$ and 0, for the three wall-normal locations, $n/L = 0.0032, 0.016$ and 0.024. The station at $x/L = -0.62$ is the

first reference location at which participants of the WMLES workshop will attempt to match their boundary-layer profiles as closely as possible to the DNS data to ensure similar upstream flow development. Prior to performing the DNS, the boundary-layer thickness at this station was estimated to have a value of about $0.032L$. Thus, the three wall-normal locations correspond to 0.1, 0.5 and 0.75 times this value, respectively. After examining the DNS data, the actual boundary-layer thickness at $x/L = -0.62$ is found to be $0.0307L$, which is fairly close to the originally estimated value.

(a) Profiles in outer units

(b) Profiles in inner units
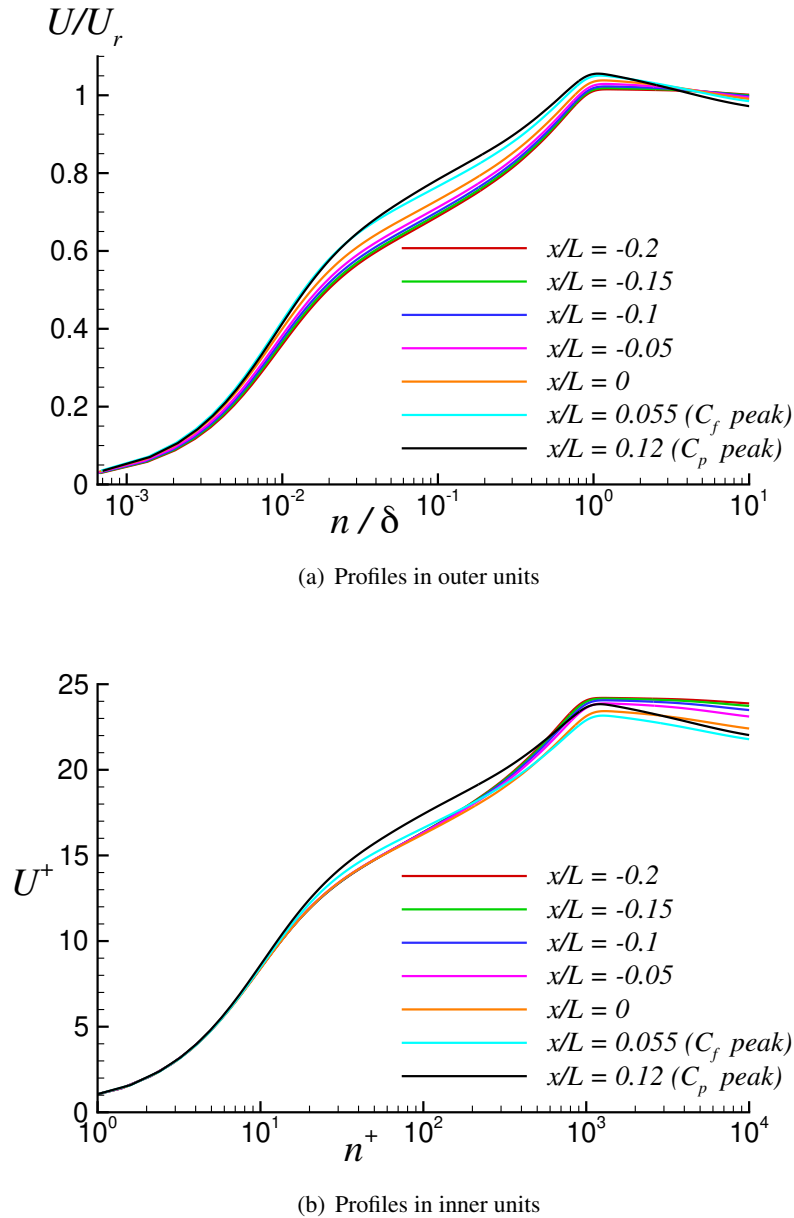
Figure 8. Mean streamwise velocity profiles in the region where $-0.2 \leq x/L \leq 0.12$.

The spectra generally display a typical relatively flat low-frequency range. At $n/L = 0.016$ and 0.024, all spectra possess an inertial range that appears to follow Kolmogorov's $-5/3$ power scaling, and extends over about a decade of frequency. The same inertial range scaling was also found in Klebanoff's incompressible flat-plate turbulent boundary-layer spectra [26, 27] taken in the wall-distance range from $0.6\,\delta$ to $0.8\,\delta$. Our spectra taken at the closest wall-normal distance, $n/L = 0.0032$, on the other hand, do not show inertial

range because of the wall interference effect at that location. The strong favorable pressure gradient, which starts at $x/L \approx -0.2$ and persists over the early ramp section, does not seem to influence the inertial range rate of decay observed at the two larger n/L locations for $x/L = -0.25$ and 0.
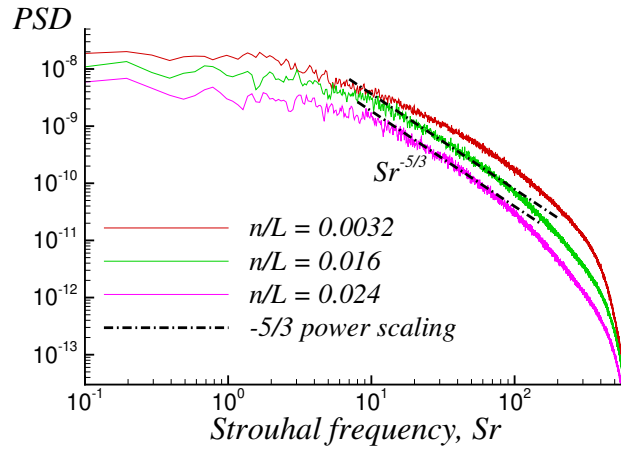
(a) $x/L = -0.62$
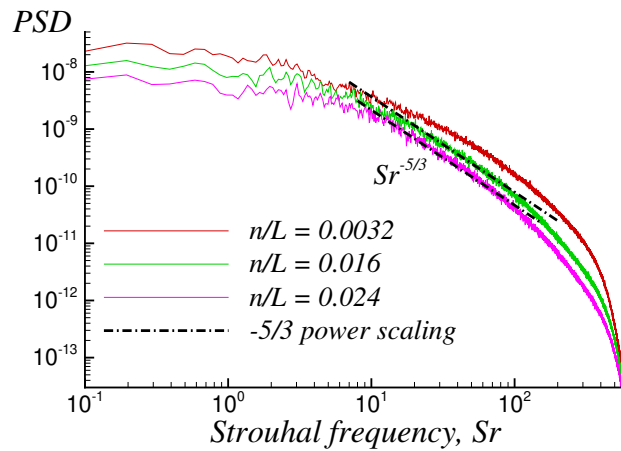
(b) $x/L = -0.25$
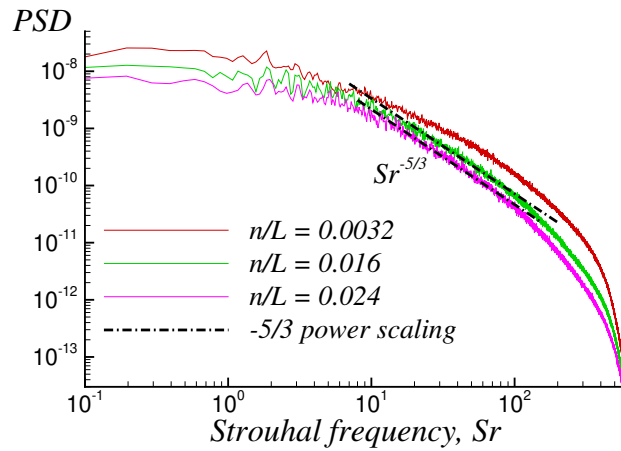
(c) $x/L = 0$

Figure 9. PSD of the axial velocity fluctuations at $x/L = -0.62, -0.25, 0$ for three n/L locations.

Figure 10 depicts the evolution of the Reynolds stress components, scaled by U_r^2, from $x/L = -0.2$ to 0.12. Here, $\langle u'u' \rangle$, $\langle v'v' \rangle$, $\langle w'w' \rangle$ and $\langle u'v' \rangle$, respectively, are the streamwise, wall-normal, spanwise and shear components of Reynolds stress in the local orthogonal system at a given station, and the $\langle \ \rangle$ operator denotes averaging in time and along the span. The wall-normal distance, n, is normalized by the local δ. The favorable pressure gradient over the shown x/L range steepens the near-wall velocity gradient in the wall-normal direction. This, in turn, increases the near-wall turbulent kinetic energy production, which also requires the presence of Reynolds shear stress. The turbulent kinetic energy production mostly occurs in the form of streamwise Reynolds stress. The energy from the streamwise component is then transferred to the other two normal Reynolds stress components by the fluctuating pressure. As seen in the figure, the streamwise Reynolds stress peak strengthens while that of the other two normal components weaken as the boundary layer becomes subjected to the strong favorable pressure gradient effect. The favorable pressure gradient interferes with the energy redistribution process, and thus affects the portion of energy transferred from the streamwise component to the other two normal components. Meanwhile, a reduction in the peak Reynolds shear stress occurs over the bulk of the acceleration region, but a reversed trend is found in the latter stages of the acceleration as the flow reaches the C_p peak at $x/L = 0.12$. The production of the Reynolds shear stress depends on the streamwise velocity gradient and the wall-normal Reynolds stress, which in turn relies on the energy transferred to it from the streamwise stress. As noted above, the production of the streamwise Reynolds stress component is dependent on the Reynolds shear stress. Hence, there is a mutual and somewhat complex dependence between the production of the turbulent kinetic energy and that of the Reynolds shear stress. In the outer part of the boundary layer, all Reynolds stress components generally show a decrease due to the stabilizing effect of the favorable pressure gradient. This is due to the gradual flattening of the outer mean velocity profile in the acceleration region, which reduces the velocity gradient there and, consequently, decreases the Reynolds stress production.

As seen in Figure 10, the peaks of the streamwise and spanwise components of the Reynolds stress are quite close to the wall, while those of the wall-normal and shear components are further away. All peaks move toward the wall as the accelerated boundary layer goes over the selected region. The shift in the streamwise and spanwise component peaks is rather minimal, while that in the other two components is more noticeable. While the peak values of the wall-normal and spanwise stresses decrease between the first and last stations of the shown x/L range, the shear stress component does not follow the same trend. The peak shear stress magnitude at the last station is about the same as that at the first station. The shear stress profile at the last station also shows the formation of a bend or a "knee point" in the vicinity of $n/\delta = 0.2$. A similar feature can also be noticed in the wall-normal and spanwise profiles at about the same n/δ for the same x/L station. These observations provide the first hints of an internal layer, whose formation is initiated by the relatively strong favorable pressure gradient encountered over the early ramp section. This particular feature will be analyzed further in the Reynolds stress profile evolutions from $x/L = 0.12$ to $x/L = 0.38$, which constitutes the deceleration region preceding the separation.

Figure 11 shows the development of the mean streamwise velocity profiles within the deceleration region. The adverse pressure gradient slows down both the near-wall and outer regions of the boundary layer, and this leads to the formation of an intermediate buffer zone that transforms into a free shear layer. The evolution of the Reynolds stress profiles in the deceleration region is shown in Figure 12. As noted in the discussion of Figure 10, the original peaks of the wall-normal and shear stress components, positioned further away from the wall, move toward the wall as the boundary layer accelerates because of the strong favorable pressure gradient. For the shear stress component, a clear near-wall peak emerges at $x/L = 0.12$, and at $x/L = 0.2$ for the wall-normal stress component. Examining all Reynolds stress profiles at $x/L = 0.2$, which is positioned in the early stages of the adverse pressure gradient, the streamwise stress peak is the closest to the wall, at $n/\delta \approx 0.013$, while the peaks of the other components are located in the vicinity of $n/\delta \approx 0.033$–0.052. We observe a weakening in the streamwise component peak as the flow decelerates toward separation, while the peaks of other stress components begin to shift outward into the emerging shear

layer. An outer peak also develops in the streamwise stress profile as the flow decelerates. The weakening of the inner streamwise stress peak is due to the reduction in the near-wall streamwise velocity gradient by the adverse pressure gradient, which lowers the streamwise stress production. The peaks in the other stress components, initially positioned relatively further from the wall, shift outward while gaining strength within the deceleration region. As the flow reaches the separation point at $x/L = 0.38$, all stress peaks are positioned close to one another at $n/\delta \approx 0.2$.

(a) Streamwise component

(b) Wall-normal component

(c) Spanwise component

(d) Shear component
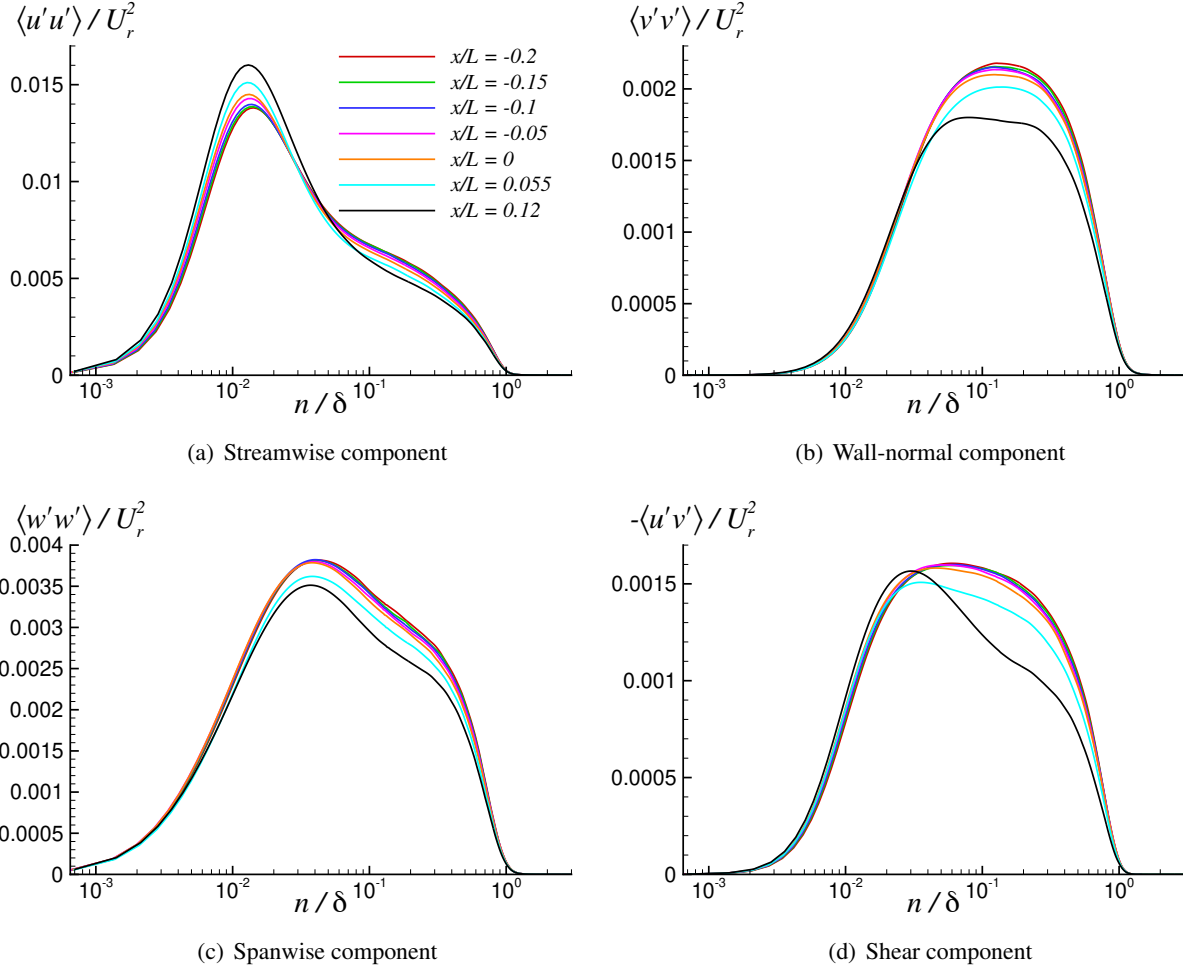
Figure 10. Evolution of Reynolds stress profiles in the region where $-0.2 \leq x/L \leq 0.12$.

Interestingly, the peak stress location at the separation point aligns well with the original n/δ location around where the knee in the Reynolds stress profiles, which hints at the formation of an internal layer, was first identified. The edge of the internal layer generated beneath the accelerated boundary layer can be taken in the vicinity of this knee point or some short distance beyond it. As the boundary layer experiences the strong favorable pressure gradient effect over a relatively brief segment in the present configuration, the edge of the internal layer developing within that region could not be determined more precisely. Nevertheless, it appears that the internal layer generated over the brief acceleration region forms the origin of the free shear layer that emerges in the deceleration region and separates. A similar observation was also made in the speed-bump flow [10], although the presence of a relatively stronger favorable pressure gradient over a much longer section made the identification of the internal layer and determination of its thickness more straightforward in that case.
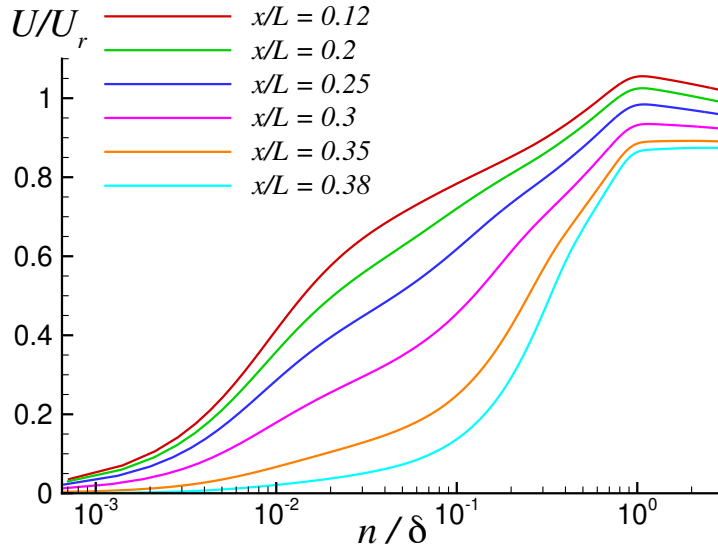
Figure 11. Mean streamwise velocity profiles in the region where $0.12 \leq x/L \leq 0.38$.
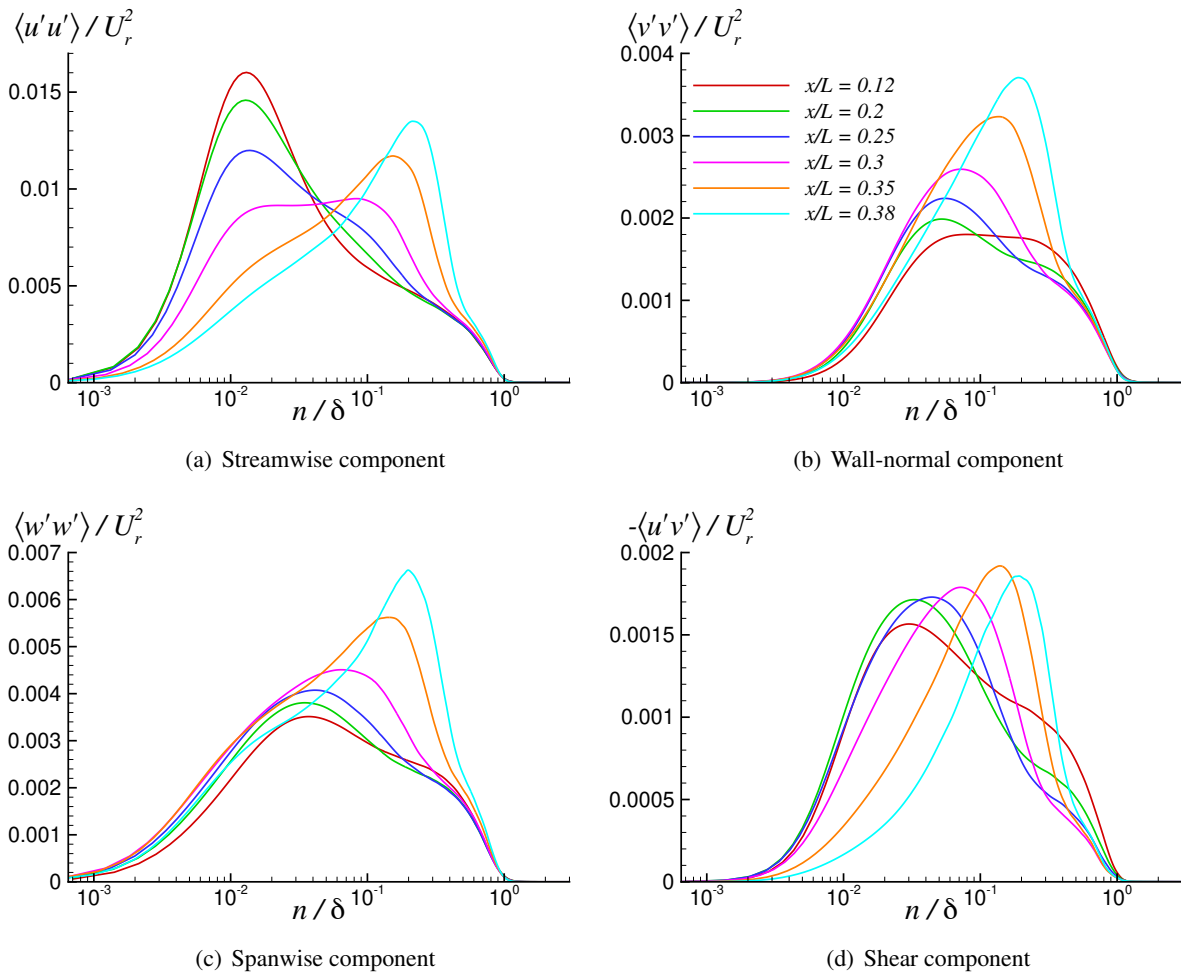

(a) Streamwise component

(b) Wall-normal component

(c) Spanwise component

(d) Shear component

Figure 12. Evolution of Reynolds stress profiles in the region where $0.12 \leq x/L \leq 0.38$.

16

Figure 13 depicts the variation of the peak values of the Reynolds stress components over the entire domain. In the weak favorable pressure gradient upstream of the ramp, the peak stresses remain fairly steady or show a gradual decrease with the streamwise distance. The peak streamwise stress begins to increase once the boundary layer interacts with the relatively stronger favorable pressure gradient near the ramp and reaches a local maximum at $x/L \approx 0.13$, which is close to the peak C_p location. The peaks of the other two normal stress components show a decrease over the same region, in accordance with the observations made in Figure 10. The peak streamwise stress starts to decrease as the flow enters the adverse pressure gradient region, while the peaks of the other two normal and the shear stress components grow, as also seen in Figure 12. The decrease in the peak streamwise stress component continues until $x/L \approx 0.3$, after which the trend is reversed. This behavior of the peak streamwise stress is the combined outcome of the weakening inner peak in the early stages of deceleration, and the emergence of a strong outer streamwise stress peak as the free shear layer develops, as seen earlier in the analysis of Figure 12. The strength of the outer peak surpasses that of the inner peak starting at about $x/L = 0.3$, which is responsible for the kink in the peak streamwise stress profile at that station in Figure 13. We observe that the peak values of the normal stress components continue to grow as the flow separates and reach their global maximum values within the detached shear layer. The peak shear stress component, on the other hand, displays an initial decrease as the flow separates before experiencing a substantial amplification in the free shear layer. The peak values of all stress components decrease once more as the separated flow reattaches and the recovery from separation begins. Further analysis of the separation and recovery regions is presented in the next subsection.
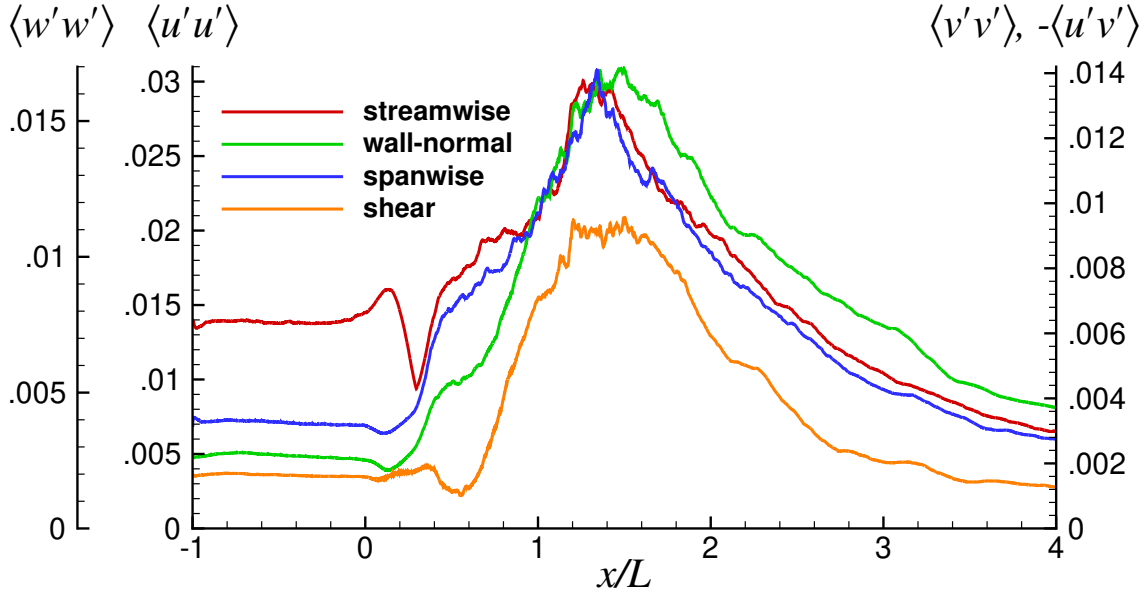

Figure 13. Variation of the peak values of the Reynolds stress components, scaled by U_r^2.

Next, we examine the two-point correlations along the span at several stations upstream of separation. The normalized correlations based on the fluctuations of the Cartesian velocity components are computed using the following expression

$$R_{ii}(x, y, \Delta z) = \frac{\langle v_i'(x, y, z) \cdot v_i'(x, y, z + \Delta z) \rangle}{\langle v_i'(x, y, z) \cdot v_i'(x, y, z) \rangle} \quad (3)$$

where v_i' denotes the fluctuation of the Cartesian velocity component v_i, i is the direction index ($i = 1, 2, 3$ indicate the x, y, z directions, respectively), Δz is the spanwise distance between the two points and the $\langle \ \rangle$ operator denotes averaging in time. The correlations at a given (x, y) are first computed separately

17

for each individual spanwise point. Because of the assumed spanwise periodicity, the data is duplicated accordingly when $(z + \Delta z)$ in the above expression exceeds $0.288L$ while z is varied from 0 to $0.288L$. The maximum value of Δz is half span or $0.144L$. All of the individual correlations are then averaged to obtain a single correlation distribution. The time history of the flowfield data gathered over $10.2L/U_r$ is used in the calculation of the correlations shown here.

Figure 14 shows the correlations in the region upstream of separation, over the range where $-0.62 \leq x/L \leq 0.375$, for three wall-normal distances from the wall. Note that the separation distance, Δz, is normalized by δ_{in}, which is a proper reference length scale for the attached flow region. The scaling by δ_{in} is also helpful for determining the minimum domain span needed upstream of flow separation. We observe that the correlations generally decay quickly and oscillate around zero after the initial decay, but with one important exception: at $x/L = 0.375$, which is slightly upstream of the separation point, for $n/L = 0.0032$, R_{11} and R_{33} maintain small negative values at relatively large separation distances. It is also interesting to note that all correlations at this particular x/L and n/L take a relatively longer separation distance to drop to zero, when compared to the other correlations taken further upstream for the same n/L. We do not find the same trends in the correlations at the larger n/L locations for $x/L = 0.375$. These observations perhaps suggest some interesting structure of the internal layer identified earlier, however further investigations would be needed to reach a better understanding of this matter. Other than the noteworthy features noted at $x/L = 0.375$ for $n/L = 0.0032$, the correlations generally approach zero by about $\Delta z/\delta_{in} = 1.5$ to 2, which means that a span of about 3 to $4\delta_{in}$ is sufficient in the region upstream of separation. The oscillatory behavior observed around zero after the initial decay of the correlations is believed to be associated with our statistical sample size, and can likely be reduced or eliminated with a longer time average.

3.2.3 *Examination of the separation and recovery regions*

We now move onto the analysis of the separated region, and the recovery zone downstream of reattachment. The mean velocity and Reynolds stress profiles in the separated region, where $0.38 \leq x/L \leq 1.45$, are shown in Figures 15 and 16, respectively. The extent of the stalled or reversed region beneath the free shear layer is denoted by the nearly zero or negative portions of the mean velocity profiles. The reversed flow region covers as much as 40% of the local δ at $x/L = 0.8$, which is roughly in the middle of the separated region. Figure 16 shows that all Reynolds stress peaks are located close to another at approximately the same n/δ location as the separated shear layer evolves. The peak stress location at the separation point initially moves away from the wall, denoted by the increasing n/δ, as the separated shear layer crosses over the recirculating flow. The peak stress location then shifts back as the separated shear layer turns back toward the wall for the reattachment at $x/L = 1.45$. As also seen in Figure 13, all normal stress peaks show substantial growth within the separated shear layer from separation to reattachment, while the shear stress component displays an initial decay in the early stages of separation, followed by a large growth.

The reversed flow region shows significant streamwise and spanwise stress levels near the reattachment point. The origin of such high levels in those two stress components can be traced back to the energetic eddies that are generated in the free shear layer. Some of these eddies that impinge on the wall in the vicinity of the reattachment point end up moving upstream along the lower wall within the reversed flow. This leads to the high levels of streamwise and spanwise Reynolds stresses near the reattachment point. These levels decrease as the distance from the reattachment point increases within the reversed flow region; this suggests that the near-wall eddies weaken as they move further upstream. There is also some increase in the level of the other two stress components in the reversed flow region near the wall, but those rises are relatively minor, as the wall-normal velocity fluctuations close to the wall are quite small.

18
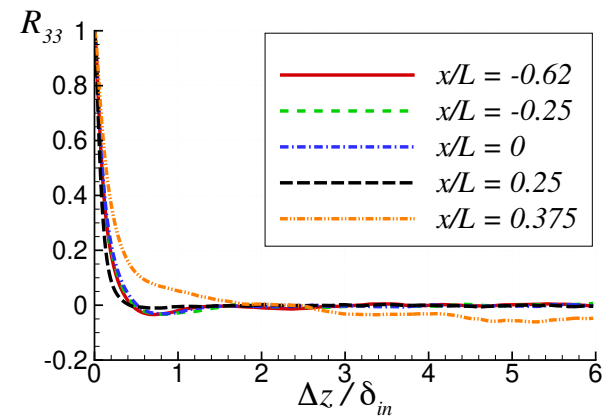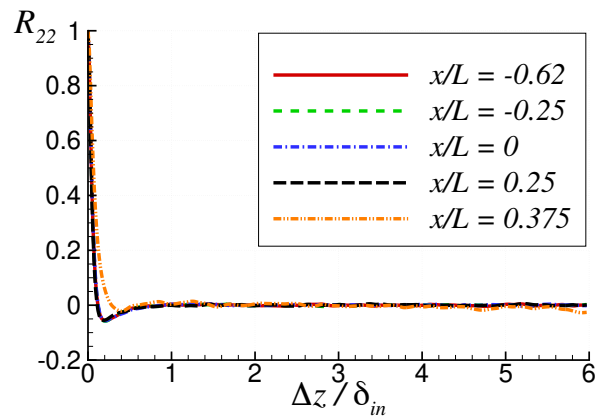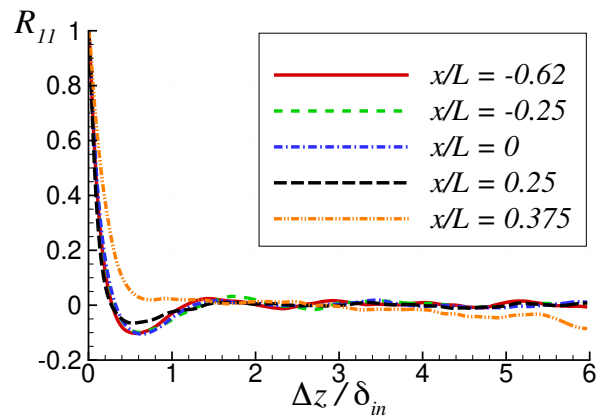
(a) $n/L = 0.0032$
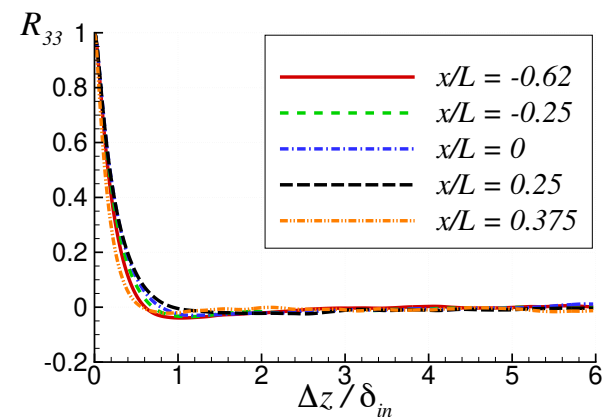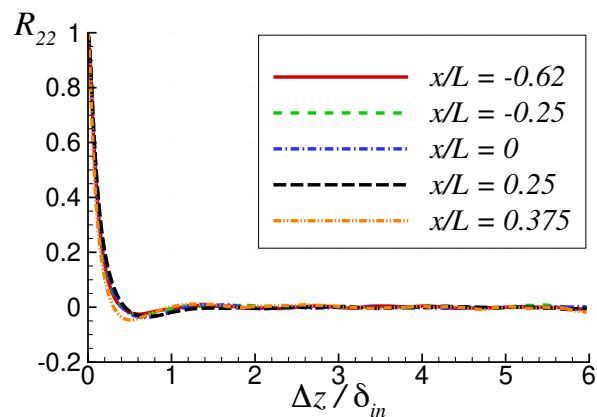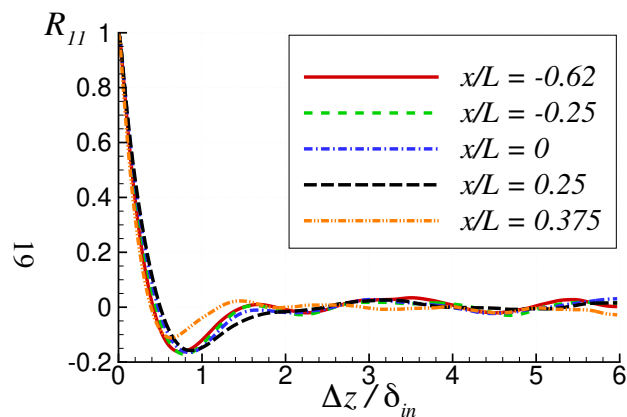
(b) $n/L = 0.016$
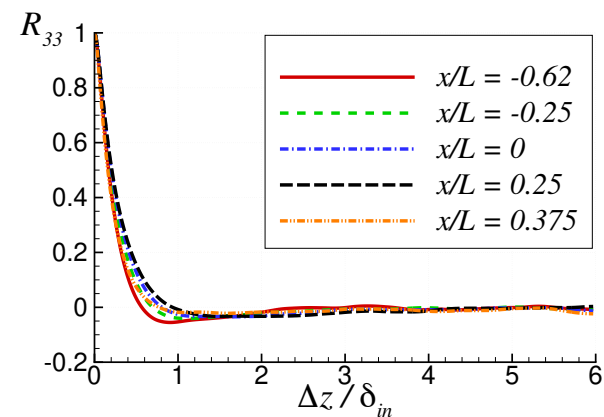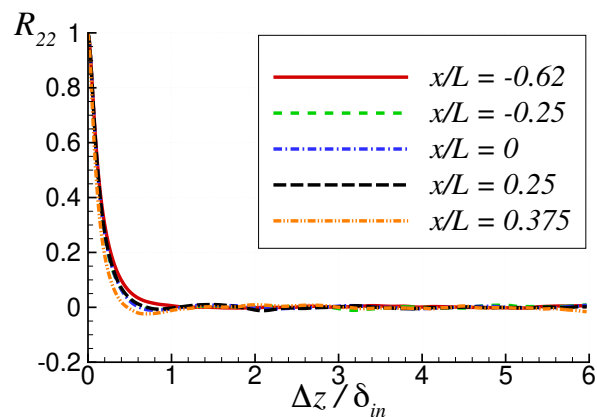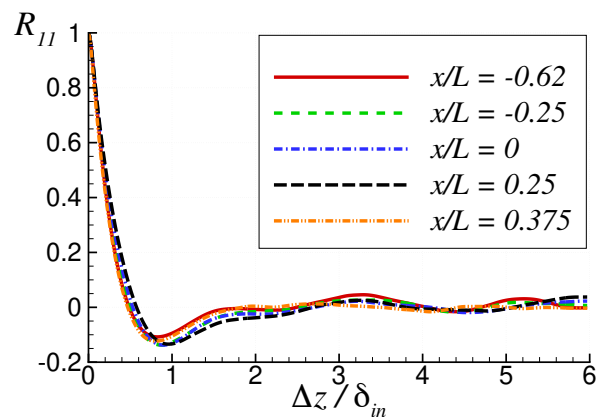
(c) $n/L = 0.024$

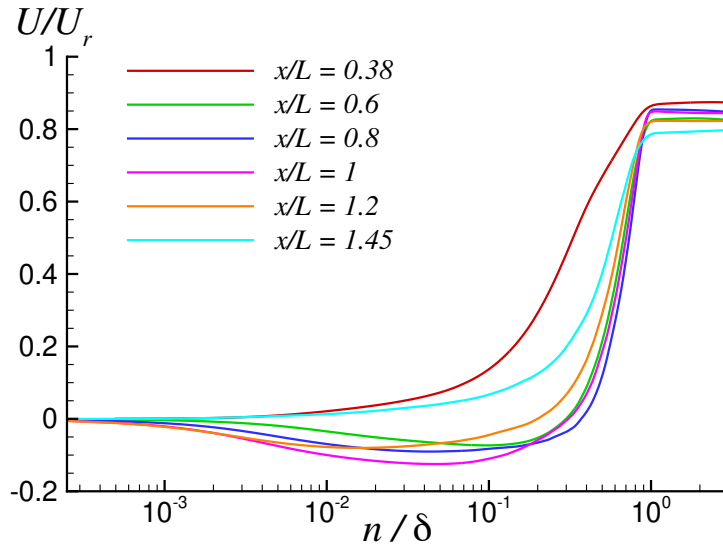**Figure 14. Two-point spanwise correlations at three n/L locations upstream of separation.**

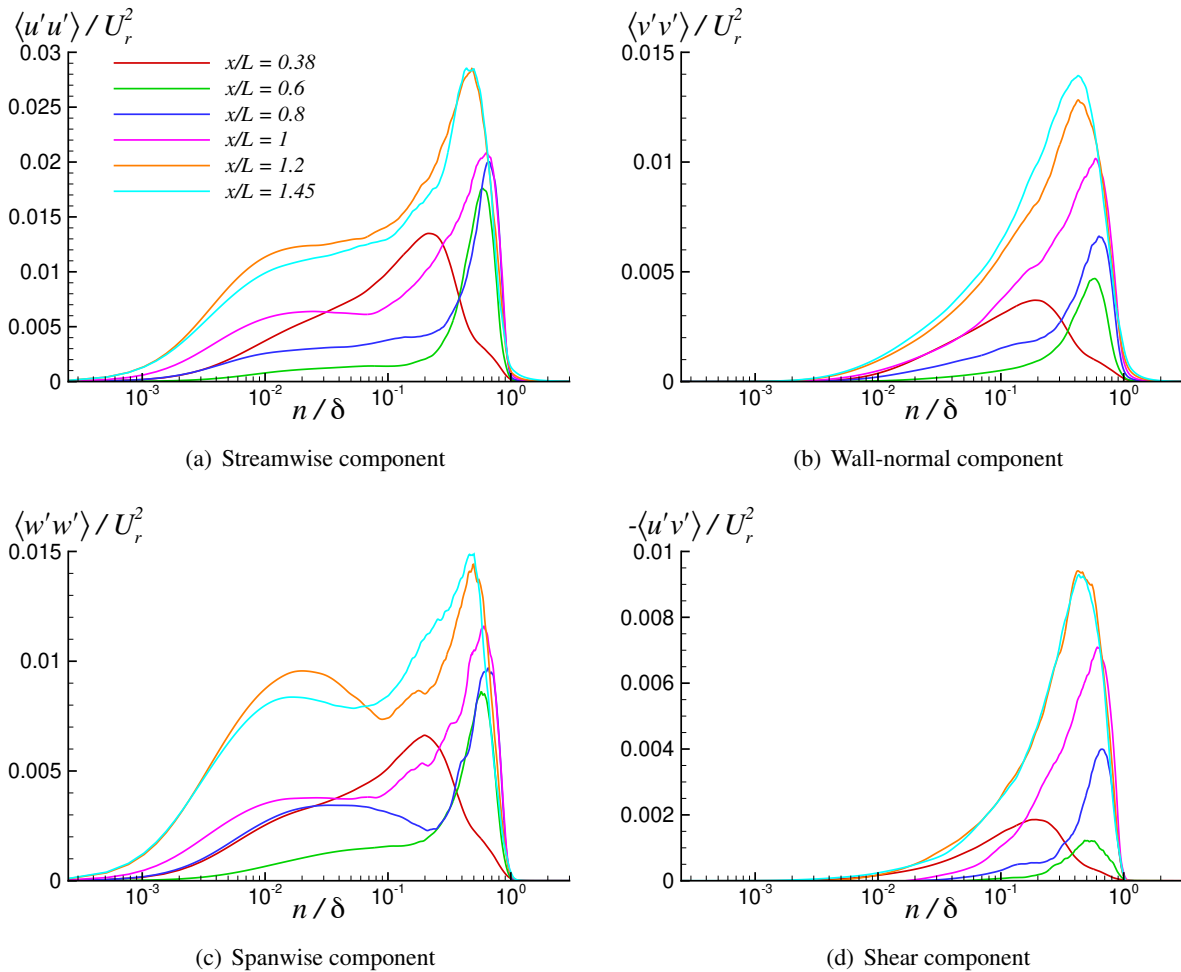**Figure 15. Mean streamwise velocity profiles in the region where $0.38 \leq x/L \leq 1.45$.**

(a) Streamwise component

(b) Wall-normal component

(c) Spanwise component

(d) Shear component

Figure 16. Evolution of Reynolds stress profiles in the region where $0.38 \leq x/L \leq 1.45$.

The development of the mean velocity and Reynolds stress profiles in the recovery zone downstream of reattachment are shown in Figures 17 and 18, respectively. The velocity profile shape at the reattachment location transforms toward the typical zero pressure gradient boundary-layer shape as the recovery flow develops under a negligible pressure gradient. The shear layer part in the reattached flow gradually disappears as the nearly zero pressure gradient of the recovery zone decreases the velocity gradient in the outer region. The primary peaks of all Reynolds stress profiles, located within the shear layer, weaken dramatically as the Reynolds stress production vanishes along with the shear layer. The considerably high levels of streamwise and spanwise Reynolds stress found near the wall within the early recovery region originate from the energetic eddies of the shear layer that impinge on the wall and travel downstream beneath the reattached flow. These near-wall structures weaken with the downstream distance and this leads to the drop in the initially high near-wall streamwise and spanwise Reynolds stress levels. As the recovery flow continues to develop further, we also observe the formation of a new inner streamwise Reynolds stress peak very near the wall, which is an indication of a new internal layer forming within the recovery flow. This internal layer is triggered by the change from the adverse to the nearly zero pressure gradient in the recovery zone. The other Reynolds stress components are also in the process of generating their corresponding inner peaks near the wall. Our physical domain is terminated at $x/L = 4$, which does not provide the necessary length for that process to complete. A longer development length is needed in order for the inner peak to complete its development in the Reynolds stress profiles. With a longer recovery domain length, the outer peaks in all Reynolds stress profiles would entirely disappear, and the inner peaks would finalize their development. The resulting mean velocity and the Reynolds stress profile shapes would be similar to those of a thick turbulent boundary layer under zero pressure gradient conditions. Therefore, for the recovery flow far downstream, the only lasting effect of the flow separation caused by the ramp would be the more than tenfold amplification of the original boundary-layer thickness.
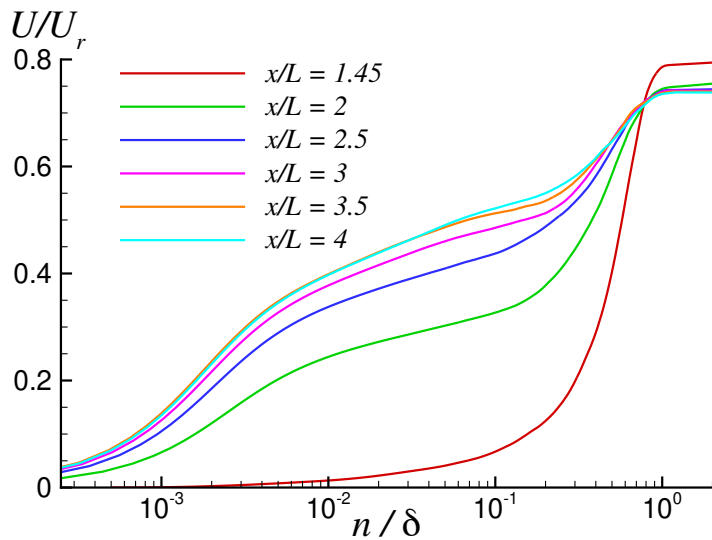

Figure 17. Mean streamwise velocity profiles in the region where $1.45 \leq x/L \leq 4$.

Figure 19 shows the two-point spanwise correlations at the vertical distance of $y/L = 0.1$ for several streamwise locations located over the range where $0.75 \leq x/L \leq 3$. This range encompasses both the separation and recovery zones. The chosen y/L position is roughly in the middle of the separated region, which contains the large-scale structures that are generated in the free shear layer and convect downstream within the reattached flow. For these correlations, the separation distance is scaled by L as that is a proper length scale for the large-scale eddies. We observe that, compared to the earlier correlations shown upstream of separation, these correlations take a considerably longer distance to decay, because of the presence of

much larger structures. Furthermore, the decay distance generally increases with the streamwise distance over the shown x/L range, indicating that the large-scale structures continue to grow in size as they convect downstream. It is also evident from the figure that a larger span is needed in order for the correlations to completely drop to zero and remain there. Hence, it can be conjectured that the relatively narrow span of the present simulation has constrained the development of large structures in the separated region, and subsequently affected the growth rate of the separated shear layer and its reattachment location. Repeating the simulation on a domain with a wider span could likely produce an upstream shift in the reattachment location, resulting from the unconstrained growth of the detached shear layer within a wider domain. It is important to note that the present DNS is designed to provide numerical data for the assessment of lower-fidelity models and is not necessarily aimed at capturing the physics of flow separation as that is much more complex in a practical situation [1], which would be currently too expensive to compute using DNS.
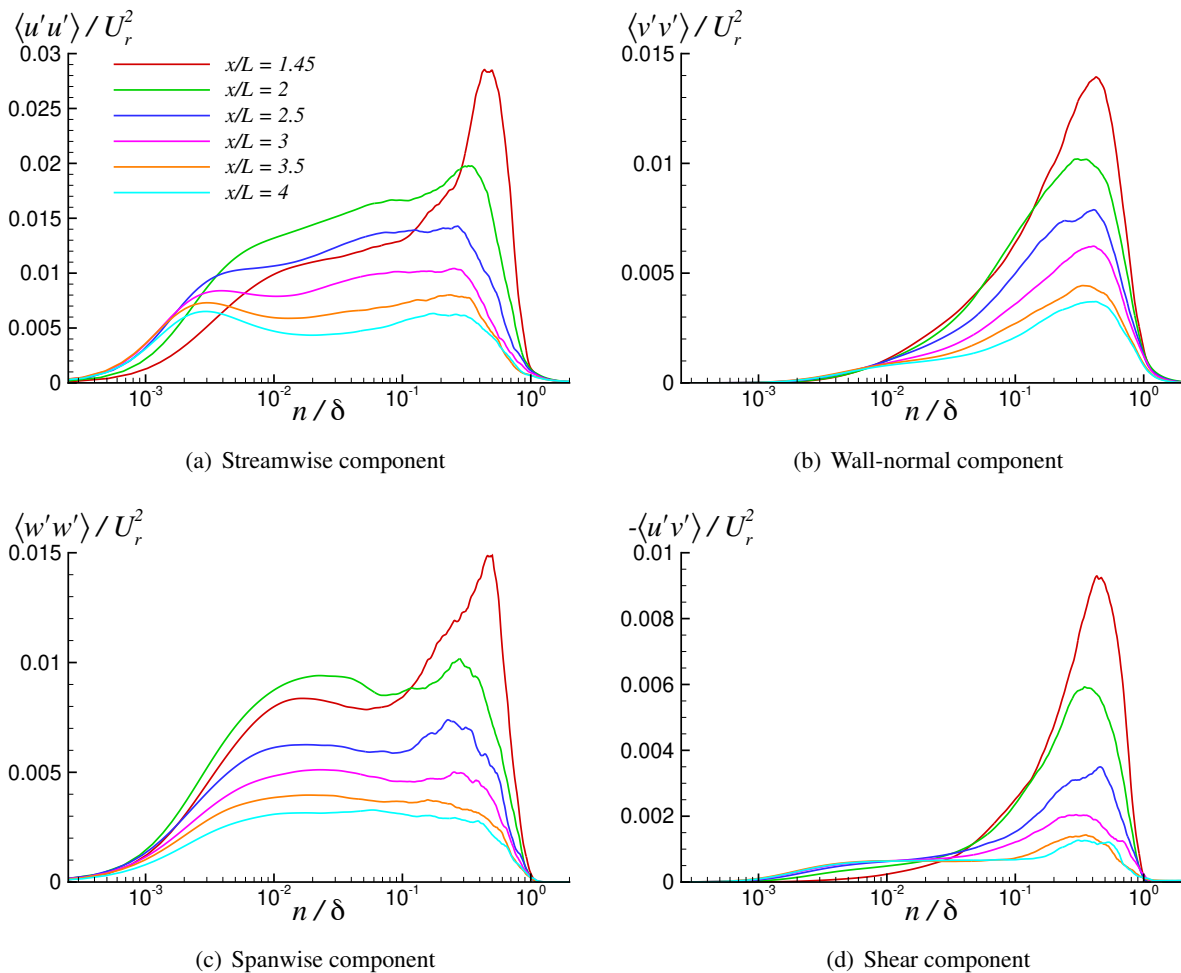

(a) Streamwise component

(b) Wall-normal component

(c) Spanwise component

(d) Shear component

Figure 18. Evolution of Reynolds stress profiles in the region where $1.45 \leq x/L \leq 4$.

Figure 20 provides the PSD of the axial velocity fluctuations at $y/L = 0.1$ for several streamwise stations over the range where $0.75 \leq x/L \leq 3$. All spectra display an inertial range with the $-5/3$ power scaling that covers more than a decade of frequency. Because of the large scale nature of the flow structures traversing the $y/L = 0.1$ location, the inertial range of these spectra start at $Sr \approx 1$. This is about one tenth of the frequency found at the beginning of the inertial range of the upstream spectra taken in the attached boundary layer, shown previously in Figure 9.
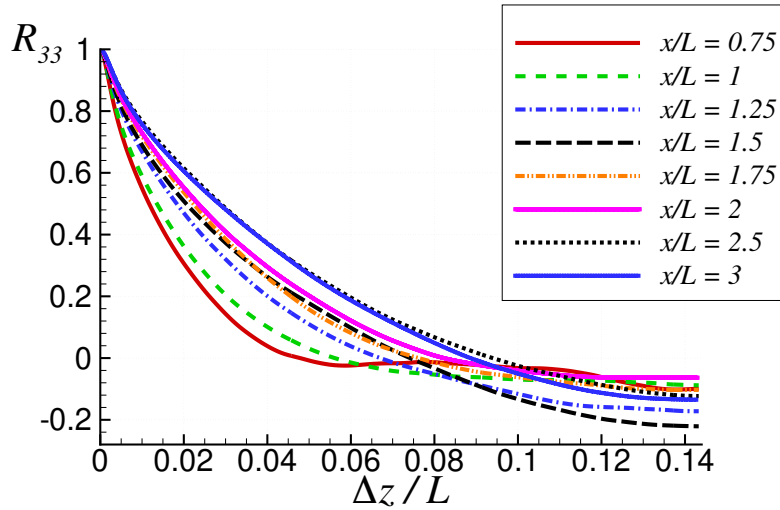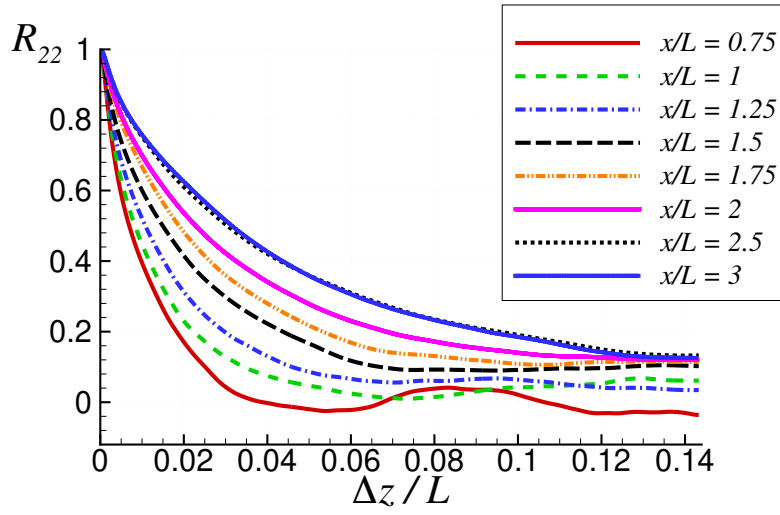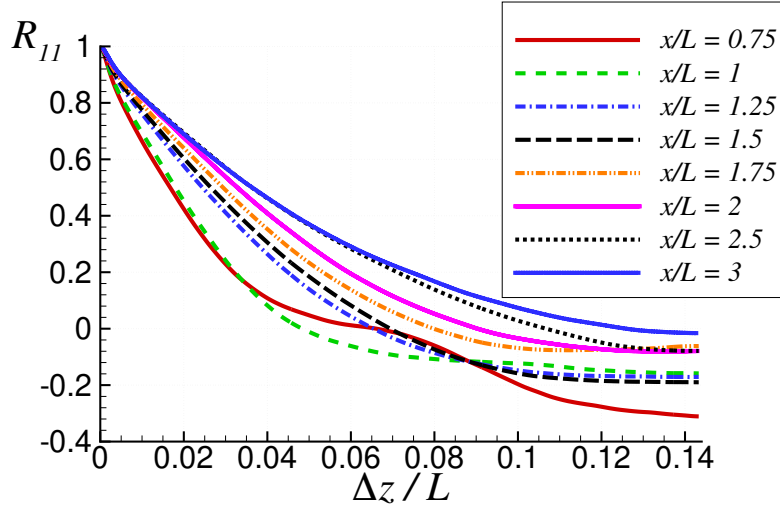
Figure 19. Two-point spanwise correlations at $y/L = 0.1$ in the region where $0.75 \leq x/L \leq 3$.
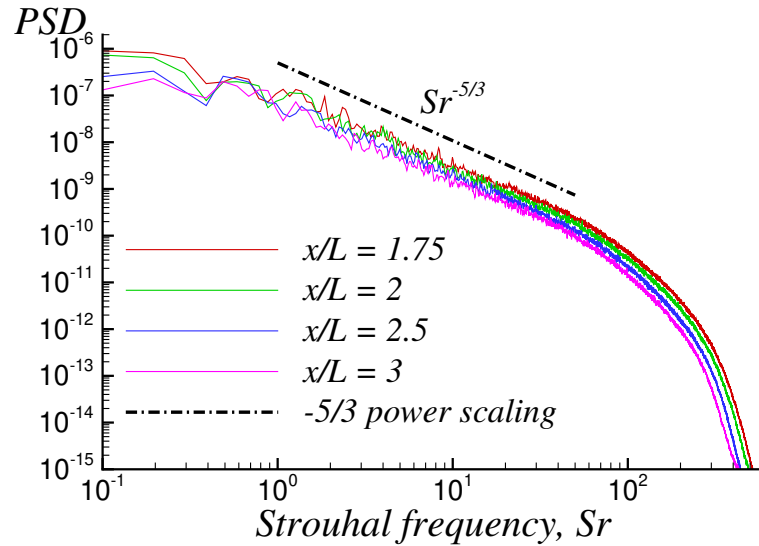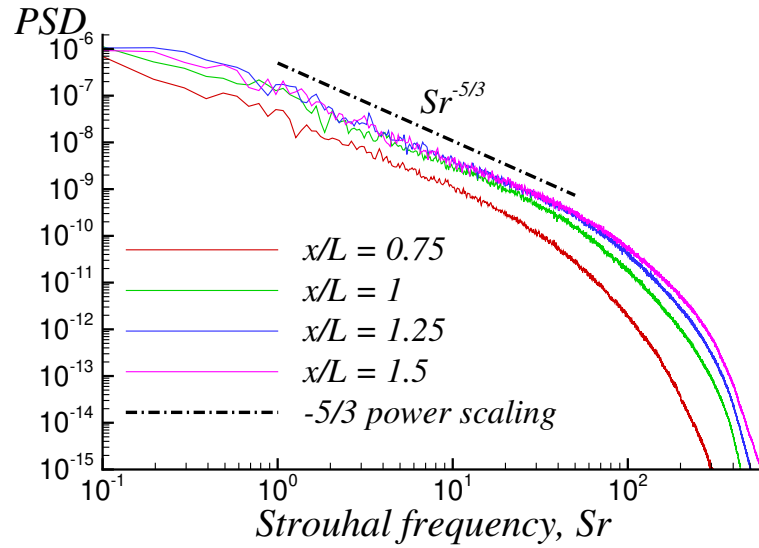
Figure 20. PSD of the axial velocity fluctuations at $y/L = 0.1$ in the region where $0.75 \leq x/L \leq 3$.

4   Concluding remarks

A spanwise-periodic direct numerical simulation of the turbulent flow past a two-dimensional smooth ramp geometry has been performed. The straight upstream section allows the incoming turbulent boundary layer to grow under a weak favorable pressure gradient. The law-of-the-wall region of the upstream profiles is similar to that of a zero pressure gradient turbulent boundary layer, while their wake region responds to the increasing favorable pressure gradient effect as the flow approaches the ramp. The turbulent boundary layer nearing the ramp first interacts with the relatively stronger favorable pressure gradient beginning at a short distance upstream of the ramp. This relatively strong favorable pressure gradient segment extends a short distance beyond the start of the ramp profile, and is succeeded by a strong adverse pressure gradient. The boundary layer subsequently experiences a modest acceleration for a brief period before decelerating and separating. Analysis of the data over this region hints at the formation of an internal layer beneath the

accelerated boundary layer. The internal layer generated over the brief acceleration region forms the origin of the free shear layer that emerges in the deceleration region and separates. Whether this particular feature of the ramp flow will create any challenges for WMLES in the prediction of separation remains to be seen.

The horizontal extent of the separated region is comparable to the ramp length, while the boundary-layer thickness near reattachment is about the same as the ramp height. The reattached flow continues to develop further under a negligible pressure gradient in the recovery region in a similar fashion to a zero pressure gradient turbulent boundary layer. The evolution of the mean streamwise velocity and the Reynolds stress profiles through the acceleration, deceleration, separation and recovery regions shows the substantial changes experienced by the flow as it goes through the various stages. The related variations in the boundary-layer thickness, displacement thickness, momentum thickness, shape factor and the boundary-layer edge velocity further illustrate the significant alterations to the mean boundary layer structure as the flow traverses the entire computational domain. For the recovery flow far downstream, the only lasting effect of the flow separation caused by the ramp is the more than tenfold amplification of the original boundary-layer thickness. The dataset generated by the present simulation can be used in the validation the WMLES studies of this flow, and other related turbulence modeling efforts aimed at improved predictions of smooth-body flow separation.

Acknowledgments

References

[1] Simmons, D. J., Thomas, F. O., Corke, T. C. and Hussain, F., Experimental Characterization of Smooth Body Flow Separation Topography and Topology on a Two-Dimensional Geometry of Finite Span, *Journal of Fluid Mechanics*, 2022, 944, A42.

[2] Larsson, J., Bermejo-Moreno, I., Garmann, D., Rizzetta, D., Baurle, R., Mukha, T., Toosi, S., Schlatter, P., Brehm, C., Ganju, S., Kahraman, A. B., van Noordt, W., Wang, Z. J., Duan, Z., Blind, M., Beck, A., Dave, S., Korobenko, A., Strasser, W., Zangeneh, R., Guzik, S., Walters, S. and Galbraith, M., Summary of the Smooth Body Separation Test Case at the 2022 High Fidelity CFD Verification Workshop, AIAA Paper 2023-1241, AIAA SciTech 2023 Forum, National Harbor, MD & Online, 2023.

[3] Slotnick, J. P., Integrated CFD Validation Experiments for Prediction of Turbulent Separated Flows for Subsonic Transport Aircraft, NATO Science and Technology Organization, Meeting Proceedings RDP, STO-MP-AVT-307, 2019.

[4] Williams, O., Samuell, M., Sarwas, S., Robbins, M. and Ferrante, A., Experimental Study of a CFD Validation Test Case for Turbulent Separated Flows, AIAA Paper 2020-0092, AIAA SciTech 2020 Forum, Orlando, Florida, 2020.

[5] Williams, O., Samuell, M., Robbins, M. L., Annamalai, H. and Ferrante, A., Characterization of Separated Flowfield over Gaussian Speed-Bump CFD Validation Geometry, AIAA Paper 2021-1671, AIAA SciTech 2021 Forum, Virtual Event, 2021.

[6] Gray, P., Gluzman, I., Thomas, F., Corke, T., Lakebrink, M. and Mejia, K., A New Validation Experiment for Smooth-Body Separation, AIAA Paper 2021-2810, AIAA Aviation 2021 Forum, Virtual Event, 2021.

[7] Gray, P., Gluzman, I., Thomas, F., Corke, T. and Mejia, K., Experimental Characterization of Smooth Body Flow Separation Over Wall-Mounted Gaussian Bump, AIAA Paper 2022-1209, AIAA SciTech 2022 Forum, San Diego, CA & Virtual Event, 2022.

[8] Uzun, A. and Malik, M. R., Simulation of a Turbulent Flow Subjected to Favorable and Adverse Pressure Gradients, *Theoretical and Computational Fluid Dynamics*, 2021, 35(3), 293–329.

[9] Balin, R. and Jansen, K. E., Direct Numerical Simulation of a Turbulent Boundary Layer over a Bump with Strong Pressure Gradients, *Journal of Fluid Mechanics*, Vol. 918, A14, 2021.

[10] Uzun, A. and Malik, M. R., High-Fidelity Simulation of Turbulent Flow Past Gaussian Bump, *AIAA Journal*, 2022, 60(4), 2130–2149.

[11] Ashcroft, G. and Zhang, X., Optimized Prefactored Compact Schemes, *Journal of Computational Physics*, 2003, 190(2), 459–477.

[12] Lele, S. K., Compact Finite Difference Schemes with Spectral-Like Resolution, *Journal of Computational Physics*, 1992, 103(1), 16–42.

[13] Gaitonde, D. V. and Visbal, M. R., Padé-Type Higher-Order Boundary Filters for the Navier-Stokes Equations, *AIAA Journal*, 2000, 38(11), 2103–2112.

[14] Visbal, M. R. and Gaitonde, D. V., Very High-Order Spatially Implicit Schemes for Computational Acoustics on Curvilinear Meshes, *Journal of Computational Acoustics*, 2001, 9(4), 1259–1286.

[15] Ekaterinaris, J. A., Implicit, High-Resolution, Compact Schemes for Gas Dynamics and Aeroacoustics, *Journal of Computational Physics*, 1999, 156(2), 272–299.

[16] Uzun, A., Hussaini, M. Y. and Streett, C. L., Large-Eddy Simulation of a Wing Tip Vortex on Overset Grids, *AIAA Journal*, 2006, 44(6), 1229–1242.

[17] Uzun, A. and Hussaini, M. Y., Investigation of High Frequency Noise Generation in the Near-Nozzle Region of a Jet Using Large Eddy Simulation, *Theoretical and Computational Fluid Dynamics*, 2007, 21(4), 291–321.

[18] Uzun, A. and Hussaini, M. Y., Simulation of Noise Generation in Near-Nozzle Region of a Chevron Nozzle Jet, *AIAA Journal*, 2009, 47(8), 1793–1810.

[19] Uzun, A. and Hussaini, M. Y., Prediction of Noise Generated by a Round Nozzle Jet Flow Using Computational Aeroacoustics, *Journal of Computational Acoustics*, 2011, 19(3), 291–316.

[20] Uzun, A. and Malik, M. R., Effect of Spatial Filtering in Implicit Large-Eddy Simulations of Separated Flows, *AIAA Journal*, 2019, 57(12), 5575–5581.

[21] Uzun, A. and Malik, M. R., Wall-Resolved Large-Eddy Simulations of Transonic Shock-Induced Flow Separation, *AIAA Journal*, 2019, 57(5), 1955–1972.

[22] Morgan, B., Larsson, J., Kawai, S. and Lele, S. K., Improving Low-Frequency Characteristics of Recycling/Rescaling Inflow Turbulence Generation, *AIAA Journal*, 2011, 49(3), 582–597.

[23] Schlatter, P. and Örlü, R., Assessment of Direct Numerical Simulation Data of Turbulent Boundary Layers, *Journal of Fluid Mechanics*, 2010, 659, 116–126.

[24] Griffin, K. P., Fu, L. and Moin, P., General Method for Determining the Boundary Layer Thickness in Nonequilibrium Flows, *Physical Review Fluids*, Vol. 6, 024608, 2021.

[25] Fernholz, H. H. and Warnack, D., The Effects of a Favourable Pressure Gradient and of the Reynolds Number on an Incompressible Axisymmetric Turbulent Boundary Layer. Part 1. The Turbulent Boundary Layer, *Journal of Fluid Mechanics*, 1998, 359, 329–356.

[26] Klebanoff, P. S., Characteristics of Turbulence in a Boundary Layer with Zero Pressure Gradient, NACA Report 1247, 1955.

[27] Schlichting, H., *Boundary-Layer Theory, Seventh Edition*, McGraw-Hill Book Company, 1979 569–570.